Modeling the chemotherapy-induced selection of drug-resistant traits during tumor growth

H. Cho[a], D. Levy[a,b,]

[a]*Department of Mathematics, University of Maryland, College Park, MD 20742, USA*
[b]*Center for Scientific Computation and Mathematical Modeling (CSCAMM), University of Maryland, College Park, MD 20742, USA*

Abstract

The emergence of drug-resistance is a major challenge in chemotherapy. In this paper we develop a mathematical model to study the dynamics of drug-resistance in solid tumors. Our model follows the dynamics of the tumor, assuming that the cancer cell population depends on a phenotype variable that corresponds to the resistance level to a cytotoxic drug. The equation for the tumor density is written as a reaction-diffusion equation with a pressure term that depends on the local cell density. The model incorporates the dynamics of nutrients and two different types of drugs: a cytotoxic drug, which directly impacts the death rate of the cancer cells, and a cytostatic drug that reduces the proliferation rate. This model successfully integrates the phenotype structured drug-resistance approach with an asymmetric tumor growth model in space. Through analysis and simulations we study the impact of spatial and phenotypic heterogeneity on the tumor growth under chemotherapy. We demonstrate that heterogeneous cancer cells may emerge due to the selection dynamics of the environment. Our model predicts that under certain conditions, multiple resistant traits emerge at different locations within the tumor. We show that a higher dosage of the cytotoxic drug may delay a relapse, yet, when this happens, a more resistant trait emerges. Moreover, we estimate the expansion rate of the tumor boundary as well as the time of relapse, in terms of the resistance trait, the level of the nutrient, and the drug concentration. Finally, we propose an efficient drug schedule aiming at minimizing the growth rate of the most resistant trait. By combining the cytotoxic and cytostatic drugs, we demonstrate that the resistant cells can be eliminated.

Keywords: Tumor growth, Drug resistance

1. Introduction

Drug-resistance to chemotherapy is a key obstacle to successful cancer treatments. The biological mechanisms responsible for the emergence of drug resistance and its propagation have been extensively studied (Gillet and Gottesman, 2010; Teicher, 2006). Those mechanisms involve genetic and/or epigenetic alternations that allow cancer cells to evade one or more drugs (Fodal et al., 2011; Gottesman, 2002; Gottesman et al., 2002). In addition, the local tumor environment, including the availability of nutrients and reduced absorption or metabolism of drugs, provides opportunities for resistant cells to evolve (Gerlinger et al., 2012; Panetta, 1998; Rainey and Travisano, 1998). The complex dynamics of the underlying mechanisms has encouraged the development of mathematical models for describing the emergence and evolution of drug resistance. Such models were used for improving early detection, quantifying intrinsic and acquired resistance cells, and designing therapeutic protocols (Foo and Michor, 2014; Lavi et al., 2012; Michor et al., 2006; Roose et al., 2007; Swierniak et al., 2009). These approaches pave a way towards a better understanding of clinical studies and experimental observations by assisting to decipher the complex mechanisms that control the dynamics of cancer under therapy.

A variety of modeling strategies have been developed to characterize tumor growth and the dynamics of drug resistance. The models range from deterministic to stochastic and from discrete to continuum models. Discrete models include cellular automata (Anderson, 2005; Mallett and De Pillis, 2006) and agent-based

*Corresponding author. Email: dlevy@math.umd.edu. Phone: 301-405-5140. Address: Department of Mathematics, University of Maryland, College Park, MD 20742-4015

Email addresses: hcho1237@math.umd.edu (H. Cho), dlevy@math.umd.edu (D. Levy)

modeling (e.g., Mansury et al. (2002)). Such models simulate individual cells, whose states are updated based on a given set of rules. Generally, it is straightforward to formulate the biological processes corresponding to tumor invasion and resistance dynamics as a discrete model. Unfortunately, such models suffer from the lack of analytical tools that can be used to analyze their properties, and the computational costs rapidly increase with an increased number of agents (cells). In larger-scale systems, continuum methods are good modeling alternatives. Such models include, e.g., ordinary differential equations (Birkhead et al., 1987; Tomasetti and Levy, 2010), partial differential equations (Anderson and Chaplain, 1998; Trédan et al., 2007; Wu et al., 2013), and integro-differential equations (Greene et al., 2014; Lorz et al., 2013).

Models based on partial differential equations have been extensively used to model cancer growth in space and time (see, e.g., Bellomo et al. (2003); Byrne et al. (2006); Cristini et al. (2008); Lowengrub et al. (2010) and the references therein). Initial modeling approaches were mostly based on reaction diffusion systems to describe the interaction between malignant and healthy cells (Gatenby and Gawlinski, 1996; Greenspan, 1976). Many extensions were proposed to include the contribution of proteolytic enzymes, stress-induced limitations, cell adhesion, microenvironment, and vascularization (Anderson, 2005; Byrne et al., 2006; Cristini et al., 2003; Deakin and Chaplain, 2013; Macklin and Lowengrub, 2007; Zheng et al., 2005).

The simplest spatial models of tumor growth assume radial symmetry. Linear and weakly nonlinear analyses have been performed to assess the stability of spherical tumors to asymmetric perturbations (Byrne et al., 2006). An extension to a fully asymmetric growth has been done by regarding the local tissue invasion of a tumor as a free moving boundary problem. To trace the boundary, various numerical techniques have been developed, e.g., boundary integral methods (Cristini et al., 2003) and advanced level-set methods (Macklin and Lowengrub, 2007), in which the nutrients are coupled with a pressure equation and a geometry-dependent jump boundary conditions. This approach was used to successfully study the effects of shape instabilities on both avascular and vascular solid tumor growth (Byrne and Chaplain, 1996; Cristini et al., 2003; Macklin and Lowengrub, 2007; Macklin et al., 2009). However, the cell pressure in these models is governed by the nutrients and the geometry without considering the competition for space that is an important factor in cancer invasion (Brú et al., 2003).

As a consequence, the concept of *homeostatic pressure*, denoting the lower pressure that prevents cell multiplication by contact inhibition, motivated a new generation of models (Byrne and Drasdo, 2009). For example, the porous medium equation was used in Kim et al. (2016); Perthame et al. (2014). Multiphase mixture models based on the theory of mixtures were proposed in Byrne and Preziosi (2003); Chaplain et al. (2006); Mcmaster et al. (2012); Preziosi and Tosin (2009). In particular, Perthame et al. (2014) used the porous medium equation to bridge the free boundary models that mostly describe the geometric motion of the tumor with cell population density models.

In parallel to developing models of tumor growth, modeling drug resistance in cancer, took a central role following the seminal works of Goldie and Coldman (1979, 1983a,b). The Goldie and Coldman models that were based on resistance due to point mutations, were extended to multi-drug resistance and optimal control of drug scheduling (Iwasa et al., 2006; Kimmel et al., 1998; Komarova, 2006; Michor et al., 2006). Recent studies emphasize the importance of the tumor microenvironment as a driving force for drug resistance (de Bruin et al., 2013; Gerlinger et al., 2012). Modeling the spatial dependency becomes more significant due to limited perfusion capability of large molecules and the differences in drug exposure based on their distance from the capillary bed (Minchinton and Tannock, 2006; Trédan et al., 2007; Vaupel P., 1989). Once spatially heterogeneous populations appear, they can also modulate the absorption and metabolism of the nutrients and drugs, which further promotes heterogeneity. Thus, various spatiotemporal models have been developed aiming at understanding the tumor morphology and phenotypic evolution driven by selective pressure from the microenvironment (Anderson et al., 2006; Panagiotopoulou et al., 2010; Trédan et al., 2007; Wu et al., 2013).

In this paper, we develop a solid tumor growth model that describes the dynamics of drug resistance. The model considers a continuous trait variable that represents the level of cytotoxic drug resistance (Cho and Levy, 2017; Greene et al., 2014; Lorz et al., 2015, 2013), which agrees with recent cytometry data analysis that reveals continuum phenotypic spaces (Amir et al., 2013; Bendall et al., 2011; Grover et al., 2016). This allows us to study the selection dynamics under microenvironmental constraints, and the response to cytotoxic and cytostatic drugs. The present model extends the framework of Cho and Levy (2017); Lorz et al. (2015, 2013) that was restricted to a radially symmetric and fixed boundary by constantly normalizing the radius. We allow the tumor boundary to take a time dependent

asymmetric shape. To model such moving boundary, we incorporate a homeostatic pressure driven growth, given by the porous medium equation (Perthame et al., 2014). The growth term is generalized to incorporate the resistance trait.

The paper is organized as follows. In Section 2, the model involving the tumor concentration and the microenvironment variables is introduced with biological assumptions. In Section 3 we use our model to analytically and numerically study the rate of the tumor growth. The time of a relapse with resistant colonies is studied in Section 4. Section 5 presents results obtained when studying tumor growth in a heterogenous environment. In Section 6 we discuss strategies to optimize the drug administration using a combination of the cytotoxic and cytostatic drug. In Section 7 we use the experiments of Mumenthaler et al. (2015) to simulate non-small-cell lung cancer and its resistance to erlotinib. Concluding remarks are provided in Section 8.

2. A model of chemotherapy for heterogeneous tumors

In this section we present our model for the dynamics of the tumor cell density $n(t, x, \theta)$. We assume a two-dimensional problem in space. The phenotype variable, $\theta \in [0, 1]$, represents the level of resistance to cytotoxic agents, with $\theta = 0$ corresponding to fully-sensitive cells, and $\theta = 1$ corresponding to fully resistant cells. We define the total cell density at each time and space location as

$$\rho(t, x) \doteq \int_0^1 n(t, x, \theta) d\theta, \tag{1}$$

and the cell pressure $p(t, x)$ in terms of cell density according to

$$p(t, x) \doteq \frac{k}{k-1} \rho^{k-1}(t, x), \tag{2}$$

with a constant $k > 1$.

The tumor growth is modeled as a porous medium-type reaction-diffusion equation

$$\begin{aligned} \partial_t n(t, x, \theta) &= G(t, x, \theta) n(t, x, \theta) \\ &+ \nu_n \Delta n(t, x, \theta) + \nu_p \nabla \cdot (n(t, x, \theta) \nabla p(t, x)). \end{aligned} \tag{3}$$

The first term on the RHS of (3) is a growth term. The reaction term governing the growth is modeled as

$$G(t, x, \theta) \doteq g(t, x, \theta)\, h(p, g), \tag{4}$$

where $g(t, x, \theta)$ is the growth rate and $h(p, g)$ is an indicator function that restricts the growth term considering the cell pressure $p(t, x)$ and homeostatic pressure $\bar{p}$. $h(p, g)$ is defined with a Heaviside function $H(\cdot)$ as follows,

$$h(p, g) \doteq 1 - H(p - \bar{p})\, H(g). \tag{5}$$

This function restricts the tumor growth when $p > \bar{p}$ and $g > 0$. We impose $\bar{p} = k/(k-1)$ to ensure that the normalized cell density is bounded as $\rho(t, x) \leq 1$.

In addition to the density of tumor cells, we model the dynamics of nutrients, $s(t, r) \geq 0$, a cytotoxic drug, $c_1(t, r) \geq 0$, and a cytostatic drug, $c_2(t, r) \geq 0$. Those quantities impact the growth rate $g(t, x, \theta)$ in (4)

$$g(t, x, \theta) \doteq R(t, x, \theta) - D(t, x, \theta) - C(t, x, \theta). \tag{6}$$

Here, $R(t, x, \theta)$ is a natural growth rate, $D(t, x, \theta)$ is a natural death term, and $C(t, x, \theta)$ is a death term due to the cytotoxic drug. The natural growth rate is taken as

$$R(t, x, \theta; s, c_2) = \frac{\varphi(\theta)}{1 + \mu_2 c_2(t, x)} s(t, x). \tag{7}$$

Here, $\varphi(\theta) > 0$ models the consumption of the nutrients depending on the resistance level. It is assumed that cells that are resistant to cytotoxic drug grow slower than sensitive cells, corresponding to $\varphi'(\theta) < 0$. The cytostatic drug $c_2(t, x)$ reduces the proliferation rate, with an uptake constant μ_2.

The natural death rate, $D(t, x, \theta; \rho)$, is assumed to be proportional to the cell density $\rho(t, x)$ with a constant death rate d, i.e., $D(\rho) = d\rho(t, x)$. Hence, our model assumes a logistic population growth.

The effect of the cytotoxic drug is modeled as

$$C(t, x, \theta; c_1) = \mu_1(\theta, c_1) c_1(t, x), \tag{8}$$

where $\mu_1(\cdot, \cdot) > 0$ is the uptake function. As the resistance level increases, the cells become more resistant to the cytotoxic drug, thus we assume that $\partial_\theta \mu_1(\cdot, c_1) < 0$. The uptake function $\mu_1(\theta, c_1)$ also depends on the cytotoxic drug c_1. This provides a more accurate description of the drug induced resistance, Cho and Levy (2017).

The second term on the RHS of (3) is a diffusion term with a diffusion coefficient ν_n. The last term on the RHS of (3) involves the cell pressure $p(t, x)$ (2). It is in the form of Darcy's law with cell velocity $\nu_p \nabla p(t, x)$. If we consider a single trait value, then $\rho(t, x) = n(t, x, \theta)$ and the last term in (3) can be rewritten as $\nu_p \Delta n^k$, which recovers the porous medium equation, Vazquez (2006).

Simpler versions of the model (3) are often used in free boundary problems, including tumor growth models, e.g., Perthame et al. (2014). In particular, the limiting behavior of porous medium PDEs with a pressure of the form (2) in the limit as $k \to \infty$ has been studied in

Kim et al. (2016); Mellet et al. (2015); Perthame et al. (2014). However, our model extends this framework to multiple trait space considering heterogeneous drug resistance and a more complex growth term that depends on the microenvironment.

The dynamics of the nutrients and drugs are modeled as a steady state reaction diffusion equation in the interior of the tumor. Thus, we first identify the boundary of the tumor as $\Omega_0 = \{x \in \Omega \,|\, n(t,x,\theta) \geq \bar{n}_0\}$ assuming a critical cell density level $\bar{n}_0$. This allows us to write the following system for $x \in \Omega_0$,

$$\nu_s \Delta s(t,x) = \left[\gamma_s + \int_0^1 \varphi(\theta) n(t,x,\theta) d\theta\right] s(t,x), \qquad (9)$$

$$\nu_{c_1} \Delta c_1(t,x) = \left[\gamma_{c_1} + \int_0^1 \mu_1(\theta) n(t,x,\theta) d\theta\right] c_1(t,x), \quad (10)$$

$$\nu_{c_2} \Delta c_2(t,x) = \left[\gamma_{c_2} + \mu_2 \int_0^1 n(t,x,\theta) d\theta\right] c_2(t,x). \quad (11)$$

Here, the ν's are the diffusion constants, and the γ's provide a decay of the corresponding terms. The boundary conditions are imposed as Dirichlet conditions on $\partial\Omega_0$,

$$s(t,x)|_{\partial\Omega_0} = S_0, \quad c_i(t,x)|_{\partial\Omega_0} = C_i, \; {}_{i=1,2}. \qquad (12)$$

Here, S_0, C_1, and C_2 model the nutrients and drug environment. They may all depend on space and time.

The resulting model (3) with (9)–(11), incorporates the nutrients and the two types of drugs into the cancer population model. This model is an extension of a simpler model that assumed a radially symmetric tumor and environment, Cho and Levy (2017); Lorz et al. (2015, 2013). In contrast to the previous works, the current model assumes a porous medium-type pressure term that controls the motion of the tumor's boundary. Such a term did not exist in the previous radially symmetric works as the boundary of the tumor was always scaled to match the boundary of the domain. Nevertheless, the results of the radially symmetric model provide motivation for studying the heterogeneous emergence of drug resistance.

The work in Cho and Levy (2017); Lorz et al. (2015, 2013) provided insights on the mechanisms that control the emergent spatial and phenotypic heterogeneity, driven by the local environment and the tumor growth. In the following section, we study the impact of spatial and phenotypic heterogeneity on the tumor growth and relapse under chemotherapy. In particular, we are interested in the emergence of heterogeneous resistant colonies.

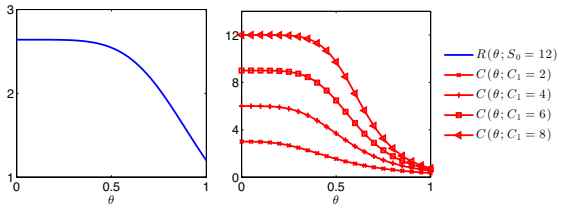

Figure 1: The natural growth rate R (left) and the drug effect C (right) in Eq. (13) as a function of the resistance level θ. $S_0 = 12$ and $C_1 = 4$.

2.1. Functional form and parameters

In order to numerically simulate the mathematical model introduced in Section 2, we take the computational domain as $x \in [-1,1]^2$, and measure the time t in days. The spatial scale is measured in centimeters considering the maximum invasion distance of the cancer cells at the early stage of invasion being approximately 1cm (Anderson, 2005). The cell density is assumed to be normalized as $\rho = 1$ with respect to the carrying capacity, for instance, using the tumor cell diameter in the range of 10^{-3}–10^{-2}cm (Melicow, 1982) or the tumor cell volume 10^{-9}–3×10^{-8}cm^3 (Casciari et al., 1992; Folkman and Hochberg, 1973) depending on the type of tumor. Also, we need to determine several terms that were left in general forms.

We start with the proliferation and drug uptake functions in Eqs. (7) and (8). These functions are assumed to be in the form

$$\varphi(\theta) = \frac{a_1}{1 + a_2\theta^5}, \qquad \mu_1(\theta, c_1) = \frac{b_1}{1 + b_2\theta^{b_3}}. \qquad (13)$$

Here, a_1 is the maximum proliferation rate per unit resource per day and b_1 is the maximum death rate per unit cytotoxic drug per day. The parameters a_2, b_2, and b_3 control the reduced proliferation rate and drug effect for the resistant traits. We take a_1, a_2, and b_1 as positive constants, while $b_2 := b_2(c_1)$ and $b_3 := b_3(c_1)$ are positive functions. The simpler choice of linear functions for $\varphi(\theta)$ and $\mu_1(\theta,\cdot)$ was shown to lead to a blowup in the phenotype distribution at the fully-sensitive or fully resistant levels (i.e., $\theta = 0, 1$) (Grothey, 2006; Lorz et al., 2015). The nonlinear dependence of the uptake function on the drug intensity effectively models the emergence of drug induced resistance and was shown to prevent the asymptotic convergence of cells to the fully-sensitive or fully-resistant states, Cho and Levy (2017). The parameters we choose for our simulations satisfy the Norton-Simon hypothesis (Simon and Norton, 2006) in which the rate of regression under chemotherapy is related to

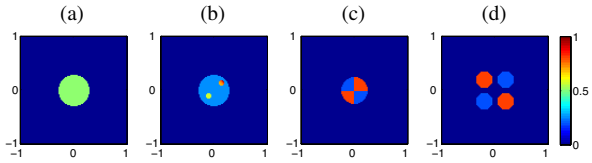

Figure 2: The mean of the resistant phenotype level in the initial density $\mathrm{E}[n_0(x,\theta)]$.

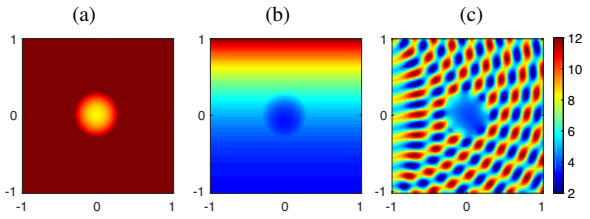

Figure 3: Examples of nutrients $s(t,x)$ with $S_0 = 12$. (a) constant; (b) diffusive; (c) highly heterogeneous.

the rate of tumor growth by

$$\frac{a_1}{1+a_2} \propto \frac{b_1}{1+b_2}. \tag{14}$$

We further follow Corbett et al. (1975); Grothey (2006) and assume that the average proliferation rate and the average mortality rate due to the effect of cytotoxic drug satisfies

$$\int_0^1 \varphi(\theta)d\theta \approx 0.2, \quad \int_0^1 \mu_1(\theta, c_1)d\theta \approx 0.8. \tag{15}$$

In particular, we choose $a_1 = 0.22$, $a_2 = 1.2$, and $b_1 = 1.5$, and the functions $b_2(c_1) = 5 + 1.25c_1$ and $b_3(c_1) = 2 + 0.5c_1$, so that the order of magnitude of these parameters are consistent with the existing literature (de Pillis et al., 2005, 2014; Lorz et al., 2015). The resource concentration is taken according to the average time for mitosis being approximately 0.3 - 1 day (Calabresi and Schein, 1993). The corresponding growth and drug effect functions are plotted in Figure 1 for $s = 12$ and different values of c_1. The cell motility constants are taken as $10^{-6} \le \nu_n, \nu_p \le 10^{-4}$ where the maximum order is chosen as $10^{-9}\mathrm{cm}^2/\mathrm{sec}$ (Bray, 2000). Other parameters are chosen similarly as in Lorz et al. (2015),

$$\mu_2 = 8, \quad \nu_s = \nu_{c_1} = \nu_{c_2} = 0.08,$$
$$d = 1.448, \quad \gamma_s = \gamma_{c_1} = \gamma_{c_2} = 1.$$

Initially, the tumor is assumed to be circular

$$n_0(x,\theta) = \rho_0\left(1 - \left(\exp\left[\frac{-\|x - x_0\|^2 - r_0^2}{\epsilon_x}\right]\right)^{-1}\right) Q_0(\theta). \tag{16}$$

Here, r_0 is the initial radius, ρ_0 is the maximum magnitude of the initial density, and ϵ_x determines the sharpness of the tumor boundary, which we set as $\epsilon_x = 0.01$. $Q_0(\theta)$ represents the initial distribution in the resistant trait space, where we either consider a truncated Gaussian with mean $\bar\theta$ and variance ϵ_θ,

$$Q_0(\theta) = \frac{1}{C_Q}\exp\left[\frac{-(\theta-\bar\theta)^2}{\epsilon_\theta}\right], \tag{17}$$

or a uniform distribution as $Q_0(\theta) = 1/C_Q$ on $\theta \in [0,1]$. In both cases, C_Q is the normalizing constant so that $\int_0^1 Q_0(\theta)d\theta = 1$. Assuming that the initial tumor is close to a single cell clone at each location in space, we set $\epsilon_\theta = 0.01$.

For distinct colonies in space, we consider a linear combination of functions in the form of Eq. (16). Figure 2 shows examples of the mean resistant trait $\mathrm{E}[n_0(x,\theta)]$ used in our simulation. In Figure 2(a), the phenotype distribution with mean $\bar\theta = 0.5$ is spatially uniform within a tumor of radius $r_0 = 0.25$. However, in Figure 2(b), a small region within the tumor is assumed to be more resistant. While the majority of the cells are taken to be distributed as Gaussian with mean $\bar\theta = 0.2$, the resistant portions are mixed with mean trait $\bar\theta = 0.7$ and $\bar\theta = 0.9$. This scenario models a tumor right after an occurrence of local mutation. To study more heterogenous cases, we consider a larger portion of resistant colonies such as those shown in Figure 2(c,d). In this case, two resistant traits of mean $\bar\theta = 0.2$ or $\bar\theta = 0.8$ are considered.

For the nutrients and drugs, we consider three different boundary conditions for Eq. (12). We first assume a constant infusion with fixed intensities S_0^b, C_1^b, and C_2^b, that is,

$$S_0(x) = S_0^b, \quad C_i(x) = C_i^b, \ _{i=1,2}.$$

Alternatively, the nutrients and drugs are diffused from the boundary resembling diffusion from a large artery. In this case, we solve

$$\nu_s^b \Delta S_0 - S_0 = 0, \quad \nu_{c_i}^b \Delta C_i - C_i = 0, \ _{i=1,2},$$

with Dirichlet boundary conditions. For instance, we impose Dirichlet conditions at the upper boundary as $S_0(x_1,1) = S_0^b$, $C_1(x_1,1) = C_1^b$, and $C_2(x_1,1) = C_2^b$, and zero Neumann conditions elsewhere. The diffusion coefficients are normalized with respect to the decay coefficient, and are chosen as $\nu_s^b = \nu_{c_1}^b = \nu_{c_2}^b = 0.25$ unless stated otherwise. Finally, we follow Peng et al. (2016) and consider a highly heterogeneous microenvironment. Given

$$w(x) = \frac{4 + \sin(8\pi\|x + (1,1)\|) + 2\sin(8\pi\|(1,-1) - x\|)}{7},$$

we set $S_0 = w(x)S_0^b$, $C_1 = w(x)C_1^b$, and $C_2 = w(x)C_2^b$. In all three cases, S_0^b, C_1^b, and C_2^b determines the (possibly time-dependent) intensity of each quantity. Figure 3(a-c) show examples of the nutrients $s(t,x)$ for the three scenarios we consider, namely, the constant, diffusive, and highly heterogeneous environment. $s(t,x)$ is computed by Eq. (9) with $S_0^b = 12$.

In our simulations, we discretize the physical space with 150 grid points and the phenotypic space with 25–50 grid points, and solve the differential equation using a fourth-order finite difference method. For the time integration, we use a fourth-order Runge-Kutta scheme with time step $dt = 0.05$. The simulation results are analyzed by the following quantities including the tumor density $\rho(t,x)$, the total number of cancer cells

$$\rho^T(t) \doteq \int_\Omega \rho(t,x)dx \gtrsim \int_{\Omega_0} \rho(t,x)dx,$$

and the relative size with respect to time t_0, i.e., $\rho^T(t)/\rho_0^T$, where $\rho_0^T = \rho^T(t_0)$. To study the trait space, we compute the mean phenotype as to quantify the dominant resistant level[1]

$$\mathrm{E}[n(t,x,\theta)] \doteq \frac{\int_0^1 \theta\, n(t,x,\theta)d\theta}{\int_0^1 n(t,x,\theta)d\theta},$$

and $\|\mathrm{E}[n(t,x,\theta)]\|_{\Omega_0}$ in case the tumor is spatially uniform.

3. Modeling tumor growth

In this section we study cancer growth with respect to the parameters that govern the tumor expansion, including the motility constants ν_n and ν_p, and the growth term $G(t,x,\theta)$.

Figure 4 shows several examples of radially symmetric tumor growth in two-dimensions for different motility constants, ν_n and ν_p at $t = 20$. The initial tumor is taken as a ball with radius $r_0 = 0.25$, and the results are computed with a single trait $\theta = 0.5$ and a constant nutrients level $S_0 = 12$. The pressure is fixed as $k = 6$. We

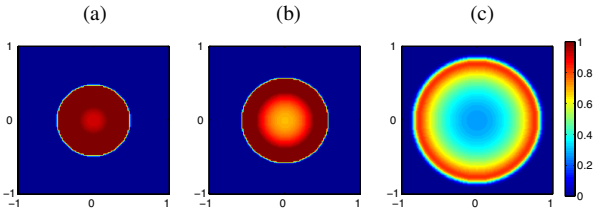

Figure 4: The tumor at $t = 20$ for different motility constants ν_n and ν_p: (a) $(\nu_n, \nu_p) = (10^{-6}, 10^{-5})$; (b) $(\nu_n, \nu_p) = (10^{-5}, 10^{-6})$; (c) $(\nu_n, \nu_p) = (10^{-4}, 10^{-6})$. The emergence of a necrotic core is observed. The corresponding cross sections are plotted in Figure 5.

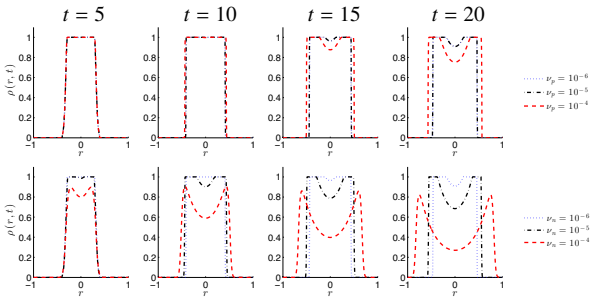

Figure 5: The cross section of a 2D radially symmetric tumor for different motility constants ν_n and ν_p. The tumor expands faster for large values of ν_n and ν_p, and ν_n contributes to the smoothness of the boundary as well.

observe that the population increases up to $\rho = 1$ and becomes restricted by the homeostatic pressure $\bar{p}$, after which it starts to expand in space. In addition, while the tumor density in the periphery is kept as $\rho = 1$, the population in the center decreases, revealing a necrotic region. For this necrotic region, it is important to note that the Heaviside function h depends on the sign of the growth rate g. The size of the necrotic region can be controlled by ν_s/γ_s.

For reference, we plot in Figure 5 the cross section of a radially symmetric tumor for different values of motility constants ν_n and ν_p. With a fixed value of $\nu_n = 10^{-6}$, Figure 5(top) shows that the tumor expands faster as ν_p increases. Similarly, the tumor grows faster for larger values of ν_n as shown in Figure 5(bottom). However, while ν_p becomes effective only when the cell pressure is large enough, ν_n governs the overall cell motility. This results with a faster expansion, as well as a smoother region in the periphery outside from where the maximum level of cell density is achieved. In the following simulations, assuming that the tumor growth is mainly driven by the pressure, we choose $\nu_n < \nu_p$, typically, $\nu_n = \nu_p/10$ with $\nu_p = 10^{-4}$, 10^{-5} and $k = 6$.

The following estimation of the tumor expansion rate can provide insights for the selection of motil-

[1] The heterogeneity in the trait space and the physical space can be computed by the variance as

$$\sigma^2[n(t,x,\theta)] \doteq \frac{\int_0^1 (\theta - \mathrm{E}[n(t,x,\theta)])^2\, n(t,x,\theta)d\theta}{\int_0^1 n(t,x,\theta)d\theta}$$

and $\left\| \left(\mathrm{E}[n(t,x,\theta)] - \|\mathrm{E}[n(t,x,\theta)]\|_{\Omega_0}\right)^2 \right\|_{\Omega_0}$, respectively. We present $\mathrm{E}[n(t,x,\theta)]$ and $\|\mathrm{E}[n(t,x,\theta)]\|_{\Omega_0}$ in this paper only when the variances are sufficiently small so that the mean is relevant to the dominating trait.

Variable/Parameter	Range	Biological interpretation
x	$[0,\ 1]^2$	Spatial variable (cm)
θ	$[0,\ 1]$	Cytotoxic drug resistance level
t	$\mathbb{R}_+$	Time (days)
$n(t, x, \theta)$	$\mathbb{R}_+$	Cell density with phenotype θ at (t, x)
$s(t, x)$	$\mathbb{R}_+$	Concentration of resources
$c_1(t, x)$	$\mathbb{R}_+$	Concentration of cytotoxic drugs
$c_2(t, x)$	$\mathbb{R}_+$	Concentration of cytostatic drugs
$\rho(t, x)$	$\mathbb{R}_+$	Total cell density at (t, x)
$p(t, x)$	$\mathbb{R}_+$	Cell pressure at (t, x)
$\varphi(\theta)$	$\mathbb{R}_+$	Proliferation rate
d	$\mathbb{R}_+$	Death rate
$\mu_1(\theta, c_1), \mu_2$	$\mathbb{R}_+$	Drug uptake rate
$\nu_n,\ \nu_p$	$\mathbb{R}_+$	Cell motility
$\nu_s,\ \nu_{c_1},\ \nu_{c_2}$	$\mathbb{R}_+$	Microenvironment permeability
$\gamma_s,\ \gamma_{c_1},\ \gamma_{c_2}$	$\mathbb{R}_+$	Microenvironment decay

Table 1: List of variables, response functions, and model parameters with their biological interpretation.

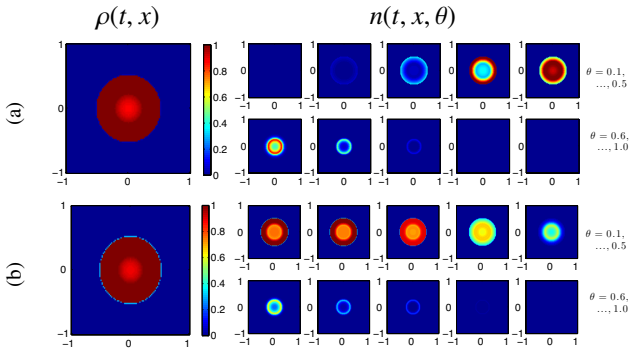

Figure 6: Cell density $\rho(t, x)$ at $t = 50$ computed with initial conditions taken as (a) a truncated Gaussian; and (b) a uniform distribution with mean $\bar{\theta} = 0.5$. The right figures show the relative density of $n(t, x, \theta)$ with fixed trait values $\theta = 0.1, 0.2, \ldots, 1.0$. While the overall density $\rho(t, x)$ is similar in both cases, the traits distribution is significantly different.

ity constants. We assume a radially symmetric tumor n_r centered at the origin with radius $r(t)$ as $\Omega_0(t) = \{x | p_r(t, x) > 0\} = B_{r(t)}(0)$. In the limit as $k \to \infty$, when $\nu_n = 0$, the speed of the boundary for the two-dimensional problem can be estimated as

$$\mathsf{v} = \sqrt{2\nu_p G(\theta)\bar{p}},$$

(see Appendix A and Perthame et al. (2014)). In this case, the tumor boundary moves proportionally to the motility constant $\sqrt{\nu_p}$ and the growth rate $\sqrt{G(\theta)}$. For nonzero ν_n, the velocity is given by

$$\mathsf{v} = \sqrt{2\nu_p G(\theta)\bar{p}} + \nu_n \int_{r(t)}^{\infty} \frac{n_r'}{s} ds + \int_{r(t)}^{\infty} n_r ds, \qquad (18)$$

where the last term vanishes in the case of $\nu_n = 0$ because $n_r = 0$ outside of the identified tumor boundary, $r(t)$. For the purpose of estimating the speed of the boundary, we neglect the contribution of the last two terms on the RHS of (18) even in the case where $\nu_n \neq 0$, as we expect this contribution to be minor.

For a heterogeneous tumor with regions of different resistance level, we claim that the cell expansion rate v can be predicted by the dominant trait. We first illustrate the nature of coexistence of multiple phenotypes embedded in our model. Figure 6 compares the cell density $\rho(t, x)$ and $n(t, x, \theta)$ of trait θ for two different initial phenotype distribution. Those are chosen as a truncated Gaussian with mean $\bar{\theta} = 0.5$ and a uniform distribution on $[0, 1]$. $n(t, x, \theta)$ is plotted for trait values $\theta = 0.1i$, $i = 1, \ldots, 10$. In both cases, the Gaussian and the uniform, the total population $\rho(t, x)$ is similar.

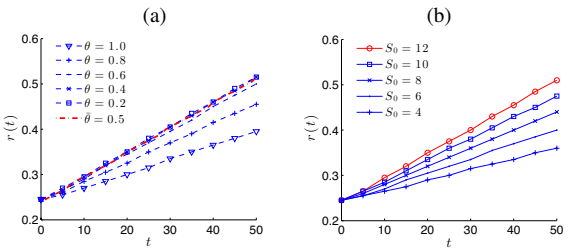

Figure 7: The growth of the radius of the tumor, $r(t)$, for different traits $\theta = 0.2, \ldots, 1.0$ (a) and nutrients level $S_0 = 4, \ldots, 12$ (b). The radius increases linearly in time.

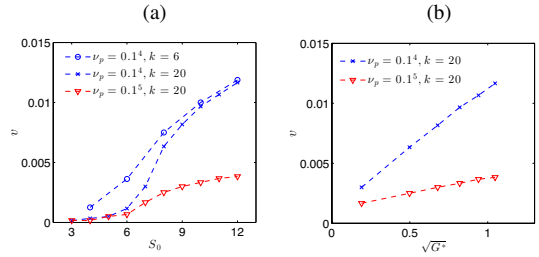

Figure 8: The speed of the tumor boundary with radius $r(t)$, $\mathsf{v} = r'(t)$ as a function of (a) the level of nutrients S_0; and (b) $\sqrt{G^*(S_0)}$. The speed of the boundary linearly depends on $\sqrt{G^*(S_0)}$.

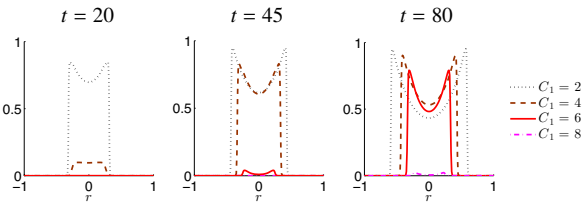

Figure 9: The cross section of a radially symmetric tumor with different drug dosages $C_1 = 2, 4, 6, 8$. The solution is shown at time $t = 20$, 45, 80. A higher dosage of the cytotoxic drug results with a late relapse.

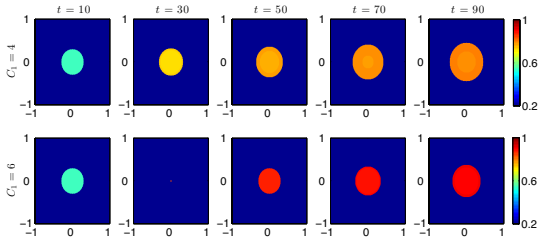

Figure 10: The evolution of the mean phenotype for drug dosages $C_1 = 4$ (top) and $C_1 = 6$ (bottom), starting from a Gaussian distribution in the trait space. A higher dose of the cytotoxic drug results with a later relapse, yet a more resistant tumor emerges.

However, in the Gaussian case, $n(t, x, \theta)$ with $\theta \approx 0.5$ occupies the largest proportion in $\rho(t, x)$, while in the uniform case, a broader range of phenotypes, mostly in the range, $0.0 \le \theta \le 0.4$, is observed.

To verify the dependency of the cell expansion rate v on the dominant trait, we compute the radius of the tumor $r(t)$ identified as $\Omega_0(t) = \{x|\rho(t, x) > 10^{-3}\} = B_{r(t)}(0)$ and its velocity $\mathsf{v} = r'(t)$. The blue lines shown in Figure 7(a) are computed with a single colony of different resistance level θ. The radius of the tumor grows linearly in time, which justifies our estimation of v. In addition, due to the form of the proliferation function $\varphi(\theta)$ that governs the growth rate $G(\theta)$, the tumor grows in a somewhat similar speed for $\theta \le 0.5$, but noticeably slower for higher resistance levels. The red line is computed with multiple colonies initially distributed as a truncated Gaussian with mean $\bar{\theta} = 0.5$ which overlaps with the lines corresponding to the sensitive cells including $\theta = 0.5$.

We also study the cell expansion rate as a function of the level of the nutrients S_0. Figure 7(b) shows that the expansion rate constantly increases as S_0 increases for $k = 6$. Figure 8 plots the slope v for different values of the parameters ν_p and k. In contrast to $k = 6$, the choice of $k = 20$ restricts the tumor growth when S_0 is not large enough so that the capacity of the logistic growth is less than 1. Thus, a tumor with its expansion strictly restricted by the pressure can be modeled with large values of k. Figure 8(b) also verifies that v is proportional to $\sqrt{\nu_p}$ and $\sqrt{G(\theta)}$. By considering the dominant trait as $\theta = 0.5$, that is, $G^* = G(0.5; S_0)$, v is proportional to $\sqrt{G^*}$ for both cases of $\nu_p = 10^{-4}$ and $\nu_p = 10^{-5}$. Also, v is almost three times larger when $\nu_p = 10^{-4}$ compared to $\nu_p = 10^{-5}$. We note that these estimates can potentially assist in determining the parameters from experiment data.

4. Studying tumor relapse with resistant colonies

In this section we study the tumor growth under treatment with a cytotoxic drug. We set $\nu_n = 10^{-6}$ and $\nu_p = 10^{-5}$. Figure 9 shows the path to a tumor relapse for different levels of cytotoxic drug dosage C_1. The initial tumor is taken to be a ball with radius $r_0 = 0.2$ and distributed as a Gaussian with mean $\bar{\theta} = 0.5$ in the trait space. We allow the tumor to grow until time $t = 10$ with $S_0 = 12$, and then apply the drug. The relapse occurs by $t = 20$, 45, 80 for drug dosages $C_1 = 4$, 6, 8, respectively. The mean phenotypes corresponding to $C_1 = 4$ and $C_1 = 6$ are plotted in Figure 10, where the dominant cells with dosage $C_1 = 6$ turns out to be more resistant compared with $C_1 = 4$.

We further study the time of the relapse in terms of the drug dosage and the resistant trait, as well as its relation with the tumor growth. For simplicity, we neglect the diffusion and growth terms. For a fixed phenotype variable θ and space location, $\rho(t) = n(t, \cdot, \theta)$ satisfies

$$\partial_t \rho(t) = (R(\theta) - D(\theta)\rho(t) - C(\theta))\, h(p, g)\rho(t), \qquad (19)$$

with initial density $\rho(t = 0) = \rho_0$. The solution to (19) can be written as

$$\rho(t) = \begin{cases} \dfrac{K\rho_0 e^{(R(\theta)-C(\theta))t}}{K + \rho_0 e^{(R(\theta)-C(\theta))t}}, & K \le 1, \text{ or } K > 1 \,\&\, t \le t_K, \\ 1, & K > 1 \,\&\, t > t_K, \end{cases}$$

with the cell capacity $K = K(\theta) \doteq (R(\theta) - C(\theta))/D(\theta)$ and $t_K \doteq (R(\theta) - C(\theta))^{-1} \ln(K/(K\rho_0 - \rho_0))$, for $K > 1$. Thus, for phenotypes such that $R(\theta) - C(\theta) > 0$, the time of relapse t_{rlps} when the total cell density $\rho(t)$ reaches the level ρ_M, can be computed as

$$t_{rlps} = \frac{1}{R(\theta) - C(\theta)} \ln\left(\frac{K\rho_M - \rho_0\rho_M}{K\rho_0 - \rho_0\rho_M}\right). \qquad (20)$$

Here, we assume that ρ_M satisfies $\min(K, 1) > \rho_M > \rho_0$, that is, the cell capacity is larger than the relapse density, which is a valid assumption for a local estimate in space. In addition, t_{rlps} is bounded below by the relapse time considering the exponential growth, that is,

$$t_{rlps} \ge \frac{1}{R(\theta) - C(\theta)} \ln\left(\frac{\rho_M}{\rho_0}\right),$$

which can be used as a lower bound. This inequality becomes sharp when $K \gg \rho_M > \rho_0$ and it depicts a clear relationship to the parameters, that is, t_{rlps} is inversely proportional to the growth rate $R(\theta) - C(\theta)$ and proportional to $\ln(\rho_0^{-1})$ depending on the preexisting resistant cells. For a time independent constant infusion of the nutrients and drug, the relapse time in terms of the drug dosages C_1 and C_2 becomes

$$\frac{1}{R(\theta; C_2) - C(\theta; C_1)} \ln\left(\frac{\frac{R(\theta;C_2)-C(\theta;C_1)}{D(\theta)}\rho_M - \rho_0\rho_M}{\frac{R(\theta;C_2)-C(\theta;C_1)}{D(\theta)}\rho_0 - \rho_0\rho_M}\right),$$

and $\partial_{C_1} t_{rlps} > 0$ and $\partial_{C_2} t_{rlps} > 0$ since $\partial_{C_2} R(\theta, C_2) < 0$ and $\partial_{C_1} C(\theta, C_1) > 0$. Thus, the time of relapse is delayed as the drug dosage increases.

For multiple colonies, if the initial phenotype distribution is uniform, the cells with phenotype

$$\Theta^* \doteq \arg\max_\theta (R(\theta) - C(\theta)) \qquad (21)$$

will increase the fastest and the cell population will be a multimodal function centered at the values in Θ^*. For non-uniform initial distributions, we can estimate the dominant phenotypes by observing the trend of

$$\Theta^* \doteq \arg\max_\theta \frac{K n_0(\theta) e^{(R(\theta)-C(\theta))t}}{K + n_0(\theta) e^{(R(\theta)-C(\theta))t}}$$

until a certain time t. Then, the relapse time will be determined by those resistant traits as

$$t_{rlps} = \min_{\theta \in \Theta^*} \frac{1}{R(\theta) - C(\theta)} \ln\left(\frac{K\rho_M - \widetilde{n}_0\rho_M}{K\widetilde{n}_0 - \widetilde{n}_0\rho_M}\right), \qquad (22)$$

where $\widetilde{n}$ is the effective initial density.

Let us include the spatial component and compute the relapse time when the total cell population reaches ρ_M^T. When the tumor is uniform in space and $\rho_M^T < area(\Omega_0) \cdot \min(K, 1)$, Eq. (22) is valid with $\rho_M = \rho_M^T / area(\Omega_0)$. Otherwise, the relapse will occur after the tumor expands. Using the expansion rate estimated from the previous section,

$$t_{rlps} = t_K + \frac{1}{\sqrt{2\nu_p G(\theta)\bar{p}}} \left(\sqrt{\frac{\rho_M^T}{\pi}} - r_0\right), \qquad (23)$$

for $K > 1$. t_K is similar to the previous estimation without the growth which is inversely proportional to $R(\theta) - C(\theta)$. In addition, the relapse time is delayed as much as the second term that is inversely proportional to $\sqrt{\nu_p}$ and to $\sqrt{G(\theta)}$ that also includes $R(\theta) - C(\theta)$. A similar relation can be obtained for $K < 1$.

We now present our numerical results and verify our estimates. Figure 11 compares the relative total number of cells $\rho^T(t)/\rho_0^T$ and the tumor radius $r(t)$ for different initial phenotype distributions. We consider three cases: a single trait $\theta = 0.5$, a Gaussian distribution with mean

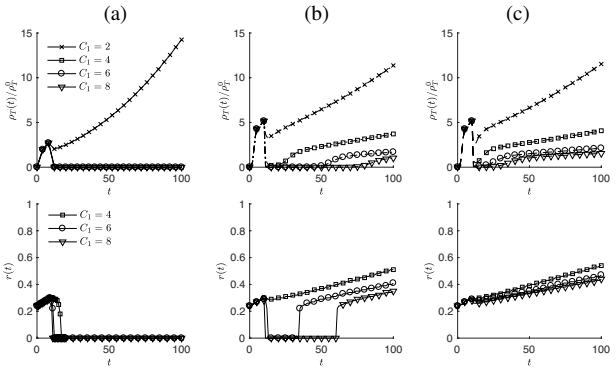

Figure 11: The dynamics of the radius of a radially symmetric tumor for different levels of drug dosage $C_1 = 2, 4, \ldots, 8$ with different initial densities. (a) single colony with $\theta = 0.5$. (b) Gaussian distribution with mean $\theta = 0.5$. (c) Uniform distribution on $[0, 1]$. (top) Relative total number of cells. (bottom) Tumor radius.

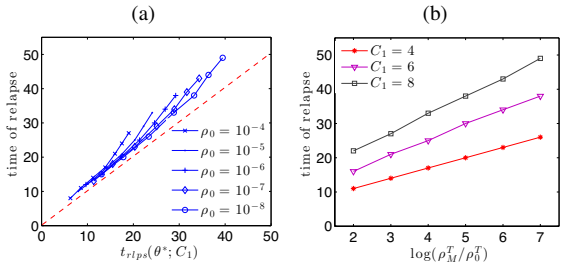

Figure 12: The time of cancer relapse for different values of the initial density and the drug dosage. (a) The time of cancer relapse t_{rlps} with respect to the drug dosages $C_1 = 3, \ldots, 8$ and the initial densities $\rho_0 = 10^{-3}, \ldots, 10^{-9}$. The estimate based on the single colony provides a lower bound for the actual time of relapse. (b) t_{rlps} as a function of $\log(\rho_M^T/\rho_0^T)$ for different dosages. A linear relation is obtained.

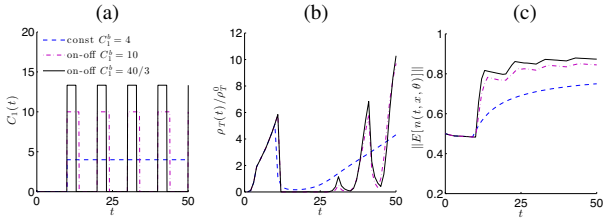

Figure 13: Comparison of a constant and on-off cytotoxic drug administration with the same total drug dosage $\int_0^{10} C_1(t)dt = 40$. (a) Drug dosage $C_1(t)$. (b) Total number of cancer cells $\rho_T(t)/\rho_T^0$. (c) Mean phenotype $\|\mathrm{E}[n(t,x,\theta)]\|$. Shorter and stronger bursts, lead to the emergence of bigger tumors during the off times, expressing more resistant traits.

$\bar{\theta} = 0.5$, and a uniform distribution on $[0, 1]$, where the proportion of resistant cells in the initial density increases in this order. Figure 11(a) corresponds to the case of a single colony with trait $\theta = 0.5$. In this case, a relapse occurs only with the lowest dosage, $C_1 = 2$. However, in both other cases, a relapse occurs even for higher drug dosages and the relapse time is delayed as the dosage increases. In the case of a uniform distribution, shown in Figure 11(c), the tumor relapses almost immediately due to a high level of preexisting resistant cells $\widetilde{n}_0$. In all cases, the slope of $r(t)$ is smaller compared with the results in the previous section, since the tumor expansion rate is reduced due to the application of drug, recalling that $\sqrt{G(\theta)}$ in v is reduced due to $C(\theta)$.

In Figure 12, we compute the time of relapse t_{rlps} for different initial densities and drug dosages. Initially the tumor is taken as a ball with radius $r_0 = 0.2$ and intensity $\rho_0 = 10^{-4}, \ldots, 10^{-8}$, uniformly distributed in the trait space. We consider the actual time of relapse when $\rho^T(t) \geq \rho_M r_0^2 \pi$ and compare it with the estimation in Eq. (22) computed with $\rho_M = 0.01$ and $\widetilde{n}_0 = \rho_0/50$. The effective initial density takes into account the trait space discretization. Figure 12(a) shows the actual time of relapse together with the estimated time according to (22). Each bullet corresponds to a different drug dosage C_1 taking $\theta^* = \theta^*(C_1)$ as the dominant trait value for each dosage as in Eq. (21). For instance, $\theta^* = 0.83, 0.95, 0.99$ for $C_1 = 4, 6, 8$. Our results show that the estimate based on a single dominant trait provides a lower bound for the actual time of relapse. In addition, Figure 12(b) verifies the expected linear relation between t_{rlps} and $\log(\rho_M^T/\rho_0^T)$.

So far we have tested our results for a time-independent drug administration. In Figure 13, we compare the constant and on-off cytotoxic drug infusion and demonstrate that the on-off schedule results in a delayed relapse, but more resistant traits (as observed in the radially symmetric model, Cho and Levy (2017)). We start the treatment at $t = 10$ with a fixed total drug dosage $\int_0^{10} C_1(t)dt = 40$ during period $T_p = 10$. Thus, for treatment lengths $T_d = 4$ and $T_d = 3$, we set the drug intensities as $C_1^b = 10$ and $C_1^b = 40/3$, respectively. The results are shown in Figure 13. Figure 13(a) shows the three different drug schedules. The relative total number of cells $\rho^T(t)/\rho_0^T$ are shown in Figure 13(b) and the mean resistance levels $\|\mathrm{E}[n(t,x,\theta)]\|$ are shown in Figure 13(c). The on-off scheme yields a delayed relapse with an increased level of resistant trait. Moreover, the total number of cancer cells reaches higher levels during the off time periods of the on-off schedules, compared with the constant drug infusion case. Overall, the drug should be administered taking into account the heterogeneity of the cancer cells. We will discuss how to design an effective drug scheme considering a combination of cytotoxic and cytostatic drugs in Section 6.

5. Modeling tumor growth in heterogeneous microenvironments

We now present simulations of cancer growth in setups that are beyond the scope of our analysis. We consider a mixture of different traits in the initial tumor and study the effect of heterogeneous nutrients and drug environment. The initial density and microenvironment intensity for our test cases are shown in Figures 2 and 3. In the remaining sections we set $\nu_n = 10^{-5}$ and $\nu_p = 10^{-4}$, Bray (2000).

Figure 14 shows the cell density $\rho(t, x)$ and the mean resistance level $\mathrm{E}[n(t, x, \theta)]$ for different cytotoxic drug dosages, corresponding to the initial density shown in Figure 2(c) with two different resistance levels $\theta = 0.2$ and $\theta = 0.8$. Similar results, corresponding to the initial density in Figure 2(d) are shown in Figure 15. The nu-

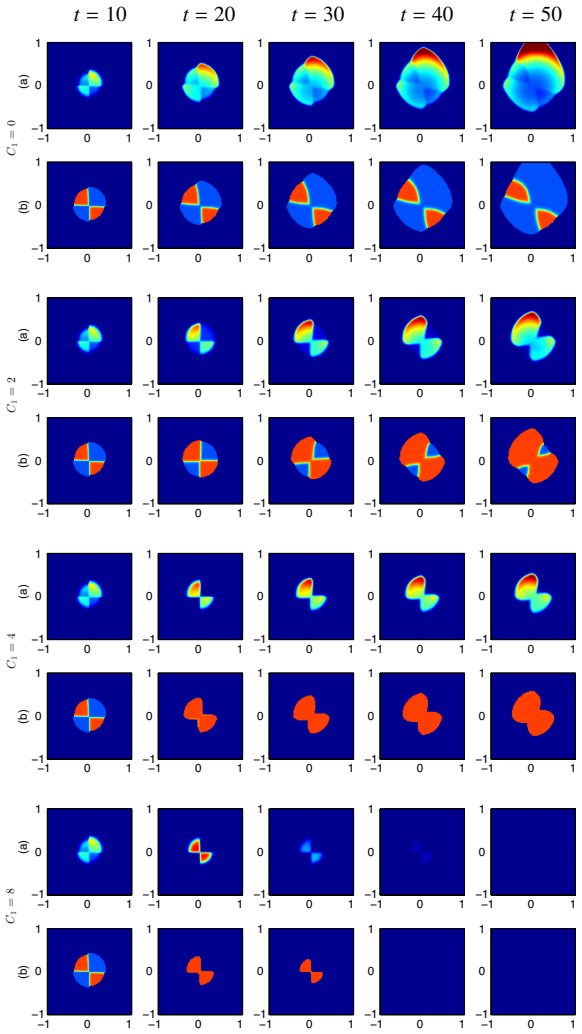

Figure 14: The dynamics of the tumor and the evolution of its traits under varying drug dosages. The initial density is given by Figure 2(c) with two different resistance levels $\theta = 0.2$ and $\theta = 0.8$, as a mixture of sensitive and resistant cells. (a) Density of cancer cell $\rho(t, x)$. (b) Mean resistant level. The nutrients and the drug are diffused from the upper boundary $x_2 = 1$ with $S_0^b = 12$ and different cytotoxic drug dosages $C_1^b = 0, 2, 4, 8$.

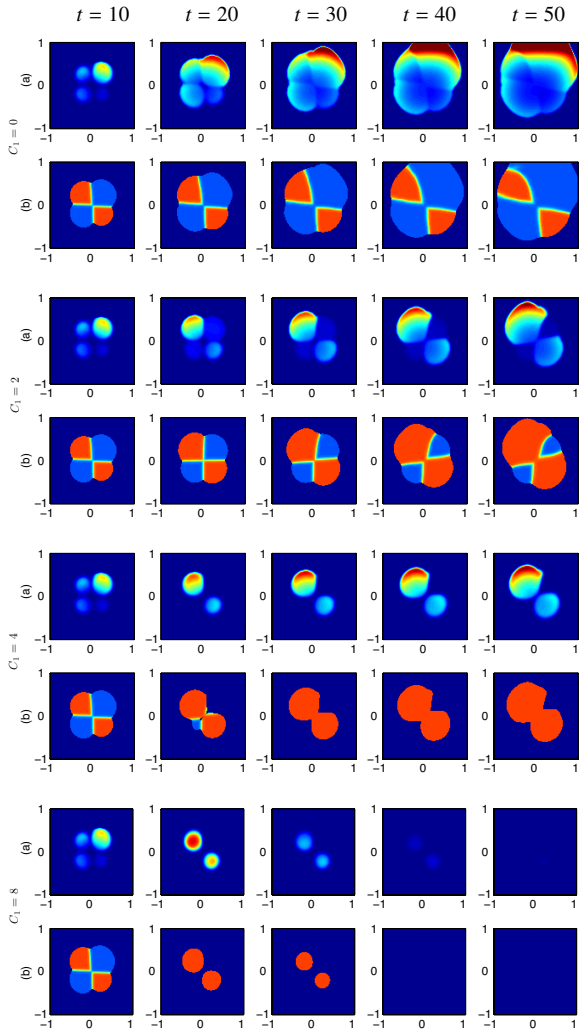

Figure 15: The dynamics of the tumor and the evolution of its traits under varying drug dosages. The initial density is given by Figure 2(d) with two different resistance levels $\theta = 0.2$ and $\theta = 0.8$, as a mixture of sensitive and resistant cells. (a) Density of cancer cell $\rho(t, x)$. (b) Mean resistant level. The nutrients and the drug are diffused from the upper boundary $x_2 = 1$ with $S_0^b = 12$ and different cytotoxic drug dosages $C_1^b = 0, 2, 4, 8$.

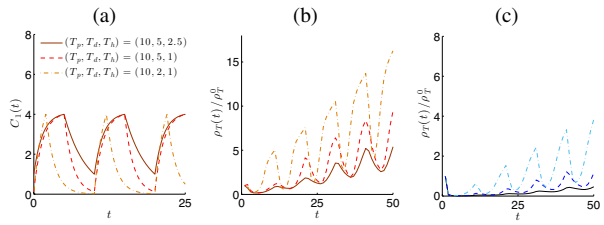

Figure 16: Time-dependent drug schedule. (a) Three protocols for $C_1(t)$ with period T_p, treatment length T_d, half-life of drug T_h, and intensity $C_1^b = 4$. (b) The total number of cells with $C_1^b = 4$. (c) The total number of cells with $C_1^b = 8$. Figures (b) and (c) correspond to the dynamics shown in Figure 17.

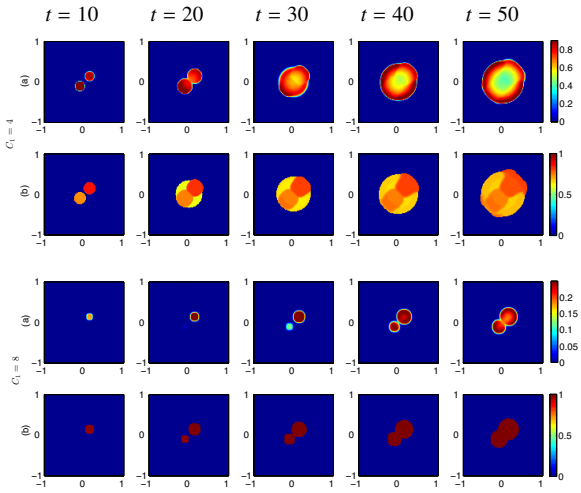

Figure 17: The dynamics of the tumor and the evolution of its traits under a time-dependent drug schedule. (a) Density of cancer cells. (b) Mean resistance level with a time-dependent infusion of cytotoxic drug $T_p = 2T_d = 4T_h = 10$ for different dosages $C_1^b = 4, 8$.

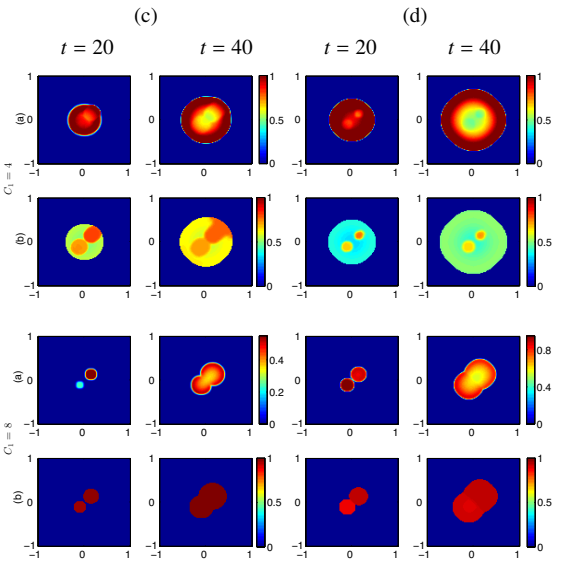

Figure 18: The dynamics of the tumor and the evolution of its traits with different time-dependent drug schedules. (a) Density of cancer cells. (b) Mean resistance level with a time-dependent infusion of cytotoxic drug: (c) $T_p = 2T_d = 10T_h = 10$; and (d) $T_p = 5T_d = 10T_h = 10$; for drug dosage $C_1^b = 4, 8$. In both cases, the tumor grows faster than Figure 17.

trients and the drug are diffused from the upper boundary $x_2 = 1$ with $S_0^b = 12$ and $C_1^b = 0, 2, 4, 8$ as in Figure 3(b), and the drug is applied at time $t = 10$. Figures 14(a) and 14(b) (also Figures 15(a) and (b)) show the dynamics of $\rho(t, x)$ and $\mathrm{E}[u(t, x, \theta)]$. In the absence of a drug, the sensitive cells grow faster and dominate the tumor. In particular, we observe a high density of cells growing near the top boundary where the nutrients has high intensity. As the drug dosage is increased, the number of sensitive cells decreases, while the resistant cells survive, and for $C_1 \geq 4$, only the resistant cells remain. The tumor vanishes when $C_1 \geq 8$, since we do not consider the resistant traits $\theta > 0.8$.

The following results are computed with a small portion of the initial population being resistant as in Figure 2(b). We consider a time-dependent drug administration as in Figure 16(a) with a period T_p, treatment length T_d, and the half-life of drug T_h (see Appendix B). The initial tumor density is assumed to be $\rho_0 = 0.5$ and the drug is infused starting at $t = 0$. Figure 17 shows the tumor growth under drug intensities $C_1^b = 4, 8$ and scheduling $T_p = 10$, $T_d = 5$, and $T_h = 2.5$. For $C_1^b = 4$, we observe that the tumor emerges at the initial location of the resistant cells. However, the cancer cells with less resistant traits also emerge in other regions at later times. With a higher drug dosage $C_1^b = 8$, only the tumor part that has sufficient amount of pre-existing resistant cells remains and starts growing. The corresponding total number of cells are shown in Figure 16(b,c). A similar pattern emerges when the ratio $T_p = T_d/2 = T_h/2$ is kept.

Figure 18 shows the dynamics of the tumor growth using different drug scheduling. Figure 18(c) corresponds to the case when the drug's half-life is reduced to $T_h = T_d/5$. Figure 18(d) corresponds to the case when the drug duration is reduced to $T_d = T_p/5$. In both cases, we observe a faster growth of the tumor, compared with Figure 17.

We proceed to demonstrate that tumors with heterogeneous resistant trait can arise even when the initial phenotype distribution is uniform in space as in Figure 2(a). Such an example is shown in Figure 19, where the initial tumor has a Gaussian phenotype distribution

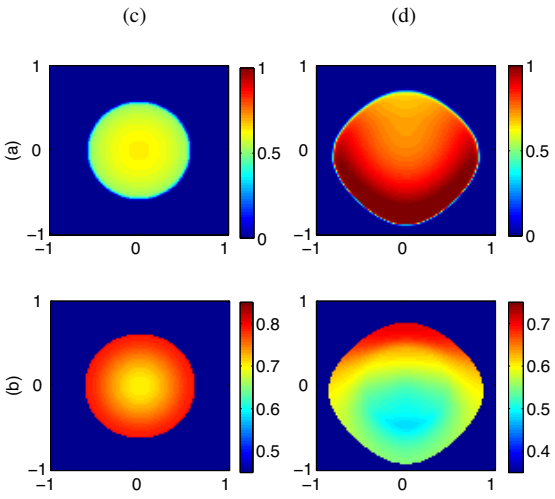

Figure 19: The emergence of heterogenous resistant traits starting from a uniform phenotype distribution. (a) Density of cancer cells. (b) Mean resistance level at $t = 40$ with (c) a constant infusion of the nutrients and the drug; and (d) infusion of the nutrients and the drug from the top boundary. These results demonstrate that a heterogeneous resistance colony can arise in different locations even when the initial state is uniform.

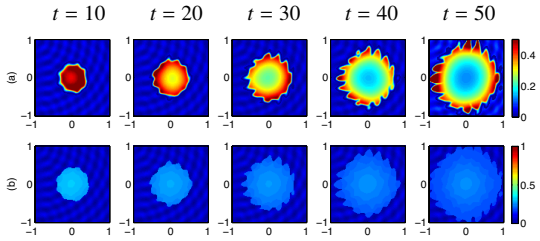

Figure 20: Tumor evolution in a highly heterogeneous nutrients environment (and no drugs). (a) Density of cancer cells. (b) Resistance level. The tumor boundary becomes irregular.

of mean trait $\bar{\theta} = 0.5$. In particular, we consider the case when the permeabilities of the drug and the nutrients differs, that is, $\nu_s/\gamma_s \neq \nu_{c_1}/\gamma_{c_1}$ in the cell interior and $\nu_s^b \neq \nu_{c_1}^b$ in the exterior environment. Figure 19(c) shows the tumor at $t = 40$ where the nutrients permeability is increased to $\nu_s = 0.25$, while $\nu_{c_1} = 0.08$. We take a constant infusion of $S_0 = 12$ and $C_1 = 4$. The population near the center of the tumor grows faster, but with a less resistant trait compared with the cells near the boundary (compare with Figure 10). Figure 19(d) presents the case when the nutrients and the cytotoxic drug are diffused from the top boundary with $\nu_s^b = 2.5$, $\nu_{c_1}^b = 0.25$, and intensities $S_0^b = 12$ and $C_1^b = 4$. The tumor grows faster further from the upper boundary where the nutrients are more diffused compared with the drug, and it is dominated by the sensitive cells. On the other hand, the tumor grows less in the upper area, but it consists of resistant cells.

Finally, we consider a highly heterogeneous nutrients and drug environment as in Figure 3(c). Figure 20 shows the cancer growth when the maximum level of the nutrients is $S_0^b = 12$ without the drugs. The relative magnitude of the nutrients environment is shown in the background of the tumor. The shape of the tumor becomes irregular since the tumor front grows faster where more nutrients are available. However, the necrotic region still has a smooth boundary. Tumor growth under

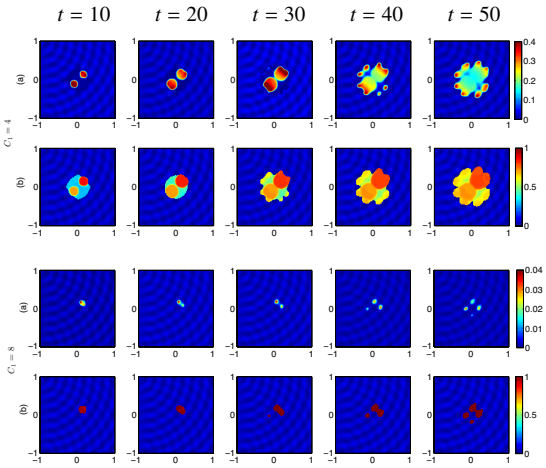

Figure 21: Tumor evolution in a highly heterogeneous nutrients environment with a time-dependent drug infusion. (a) Density of cancer cells. (b) Resistance level. The drug is administered with $T_p = 2T_d = 4T_h = 10$ and dosages $C_1^b = 4, 8$.

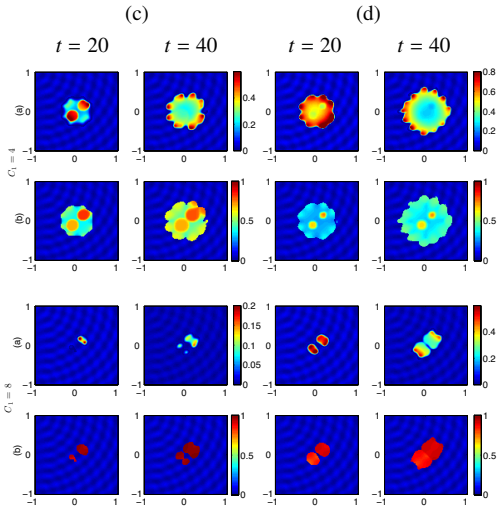

Figure 22: Tumor evolution in a highly heterogeneous nutrients environment with a time-dependent drug infusion. (a) Density of cancer cells. (b) Resistance level. The drug is administered with (c) $T_p = 2T_d = 10T_h = 10$; (d) $T_p = 5T_d = 10T_h = 10$, and dosages $C_1^b = 4, 8$.

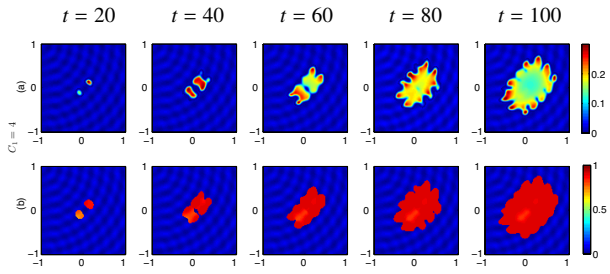

Figure 23: Long time evolution of the tumor with a heterogeneous infusion of nutrients and drug until $t = 100$. (a) Density of cancer cells. (b) Resistance level. The scattered tumor grows into a single resistant patch at later times.

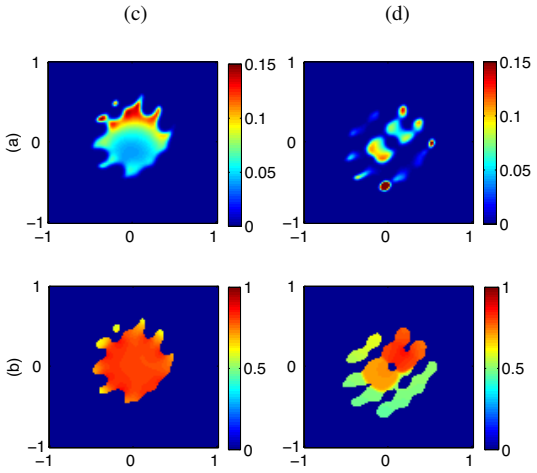

Figure 24: Tumor evolution in a highly heterogeneous environment at $t = 40$. (a) Density of cancer cells. (b) Mean resistance level. (c) Nutrients diffuse from the upper boundary in a highly heterogeneous drug environment. (d) The drug diffuses from the upper boundary in a highly heterogeneous nutrient environment. Cancer cells with distinct resistant trait arise in different location.

the infusion of time-dependent scheduling with different drug treatment period T_d and drug half-life T_h is shown in Figures 21 and 22. For $C_1^b = 4$, the results are similar to the constant infusion case except for the irregular boundary and slightly more heterogeneous colonies. However, with a higher drug dosage of $C_1^b = 8$, the tumor grows in a scattered pattern with highly resistant cells. Figure 23 shows the cancer growth for a longer period until $t = 100$. Here, we take a time-independent dosage with a constant level $C_1 = 4$. The scattered tumors eventually merge, aligning with the nutrients environment.

In addition, we present two examples where distinct patterns of heterogeneous tumors emerge. The nutrients and the drug intensity are set as $S_0^b = 12$ and $C_1^b = 4$. Figure 24(c) corresponds to the case of a nutrient that is diffused from the upper boundary in a highly heterogeneous drug environment. We observe distinct levels of resistant traits between the cells in the tumor interior and on the tumor boundary. The latter consists of less resistant cells. Figure 24(d) corresponds to the case when the nutrients are highly heterogenous and the drug diffuses from the top of the domain. The tumor grows in a scattered pattern with distinct resistance levels emerging in different locations.

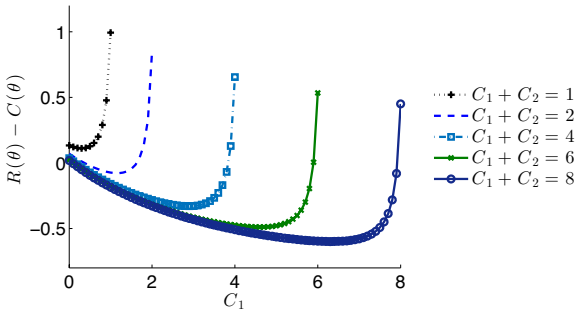

Figure 25: Growth rate $R(\theta^*; C_2) - C(\theta^*; C_1)$ of the most resistant trait $\theta^* = 1$ for different cytotoxic and cytostatic drug dosages, C_1 and C_2, respectively. Each line corresponds to a fixed value of $C_1 + C_2 = \mathbf{c}$ and the maximum decay rate is achieved where C_1 is slightly less than $\mathbf{c}$.

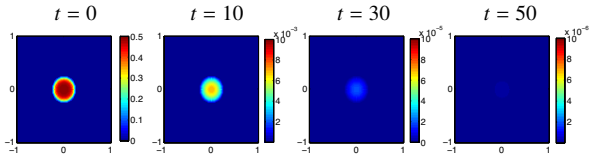

Figure 26: Density of cancer cells, starting from a tumor with a Gaussian phenotype distribution, treated with the optimal drug dosage for the case $C_1 + C_2 = 2$ as in (24). The tumor constantly shrinks and does not relapse.

6. Modeling optimized drug scheduling

In the previous sections we demonstrated that due to the preexisting resistant cells, a relapse is unavoidable regardless of the dosage of the cytotoxic drug. A common approach is therefore to combine drugs that target different mechanisms. In this section we propose a strategy of combining cytotoxic and cytostatic drugs. While the cytotoxic drug, C_1, directly impacts the death rate of the cancer cells, the cytostatic drug, C_2, reduces the proliferation rate.

The general drug scheduling optimization problem is complex, and is beyond the scope of this paper. Here, we aim at a simpler problem, in which for a fixed total drug concentration $C_1 + C_2$, we look for the dosage that minimizes the growth rate of the most resistant trait $\theta = 1$. Let us assume a constant infusion of C_1 and C_2. Then the growth rate of the tumor with trait θ^* at the boundary becomes

$$R(\theta^*; C_2) - C(\theta^*; C_1) = \frac{r(\theta^*)S_0}{1 + \mu_2 C_2} - \mu_1(\theta^*, C_1)C_1 = \frac{\bar{r}_1 S_0}{1 + \bar{\mu}_2 C_2} - \frac{\bar{\mu}_1^1}{\bar{\mu}_1^2 C_1 + \bar{\mu}_1^3} C_1,$$

where $\bar{r}_1$, $\bar{\mu}_2$, $\bar{\mu}_1^1$, $\bar{\mu}_1^2$, $\bar{\mu}_1^3$ are constants from our choice

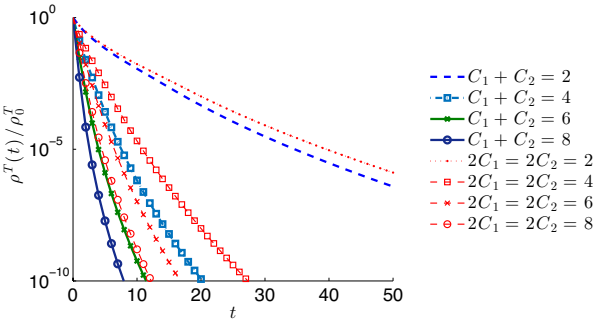

Figure 27: Total number of cancer cells $\rho_T(t)/\rho_T^0$ with different drug schedules. The thick lines correspond to the result with the optimal dosage $C_1 + C_2 = \mathbf{c}$ given by (24). The thin lines are with an equal dosage $C_1 = C_2 = \mathbf{c}/2$. The optimal dosage results with a faster shrinkage of the tumor.

of system parameters that are specified in Section 2.1. Thus, in order to shrink the tumor, we require a dosage for which $R(\theta^*; C_2) - C(\theta^*; C_1) < 0$ for all θ^*. In addition, assuming a constant total drug dosage $\mathbf{c} = C_1 + C_2$, the minimizer of the growth rate at $\theta^* = 1$ can be computed as

$$C_1 = \frac{\bar{\mu}_2 \mathbf{c} + 1 - A\bar{\mu}_1^3}{\bar{\mu}_2 + A\bar{\mu}_1^2}, \qquad C_2 = \mathbf{c} - C_1, \tag{24}$$

where $A = \sqrt{\bar{\mu}_2 \bar{r}_1 S_0 / \bar{\mu}_1^1 \bar{\mu}_1^3}$. This can be further extended to adapting the dosage according to the dynamics of the dominant trait.

Figure 25 shows the growth rate $R(\theta^*; C_2) - C(\theta^*; C_1)$ for different level of total drug dosage $\mathbf{c} = 1, 2, 4, 6, 8$ with respect to the cytotoxic dosage C_1. Each curve corresponds to a fixed value of $\mathbf{c}$ and the cancer cells decay when $\mathbf{c} \geq 2$. The right endpoint of each curve corresponds to the case of using the cytotoxic drug $C_1 = \mathbf{c}$ only. It illustrates that when only the cytotoxic drug is applied, the most resistant cells have a positive growth rate. However, adding the cytostatic drug resolves this issue. The growth rate becomes negative as we move left on the curve, and the maximum decay rate, (24), is achieved. We denote this as the optimal drug dosage and use it in the following simulations.

We first consider the time independent constant infusion for both the cytotoxic and cytostatic drug. Figure 26 shows the density of the tumor that is initially uniform in space with a Gaussian phenotype distribution of mean $\bar{\mu} = 0.5$. We apply the drug with a fairly low dosage, $\mathbf{c} = 2$. In contrast to the results in section 4, the tumor constantly shrinks and the relapse does not happen. The total number of cells $\rho^T(t)/\rho_0^T$ for different drug schedules are shown in Figure 27. In addition to

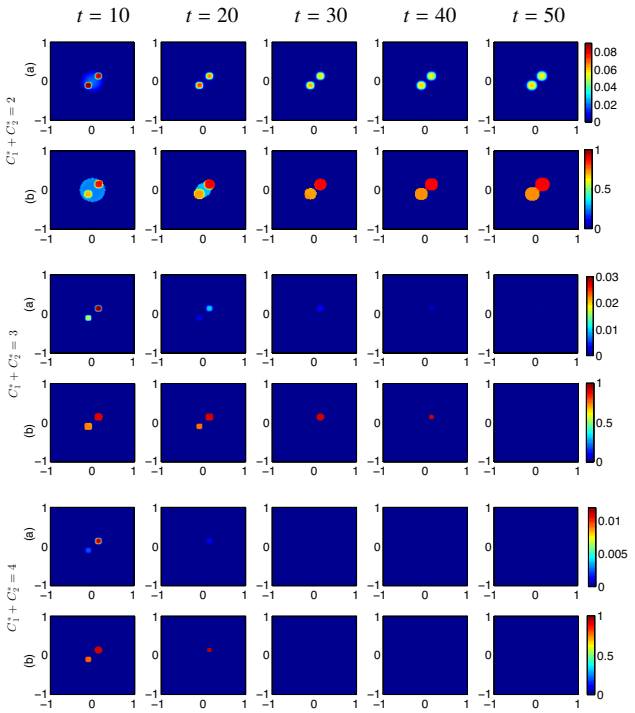

Figure 28: (a) Density of cancer cells $\rho(t, x)$. (b) Mean resistance level. The initial tumor consists of a mixture of sensitive and resistant cells. The cytotoxic drug is given as $T_p = 2T_d = 4T_h = 10$ and the cytostatic drug is provided as a constant infusion. Using the drug intensity computed by our optimal dosage, the tumor can be eliminated without a relapse.

the optimal drug dosage using $\mathbf{c} = 2, 4, 6, 8$, we also present the case of an equal dosage of $C_1 = C_2 = \mathbf{c}/2$. We verify that for a fixed $\mathbf{c}$, the optimal dosage (24) indeed provides a better decay rate.

Next, we test the outcome when the initial tumor includes a small region that is dominated by the resistant cells as in Figure 2(b). We apply a time-dependent dosage with a period $T_p = 2T_d = 4T_h = 10$ for the cytotoxic drug, and a time independent constant dosage for the cytostatic drug. The effectiveness of such drug schedule has been demonstrated for a simpler model in Lorz et al. (2015). We apply the drugs as follows. We denote the case $C_1^\star + C_2^\star = \mathbf{c}$ being comparable to the dosage $C_1(t)$ used in Figure 16(a) with $C_1^b = \mathbf{c}$, i.e., $\int_0^{10} C_1^\star(t) + C_2^\star(t)dt = \int_0^{10} C_1(t)dt$. Still, the intensities of the drugs are computed by (24). The tumor density and the corresponding resistance levels are plotted in Figure 28. The total number of cells is plotted in Figure 29. Once again, this demonstrates that a relapse can be prevented by our proposed strategy, and it can be completely eliminated with $C_1^\star + C_2^\star \gtrapprox 3$.

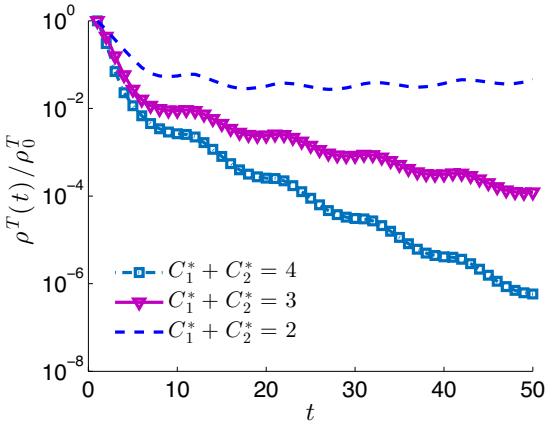

Figure 29: Total number of cancer cells $\rho_T(t)/\rho_T^0$ corresponding to Figure 28.

7. Simulation of non-small-cell lung cancer and resistance to erlotinib

Erlotinib is a targeted drug used to treat non-small cell lung cancer (NSCLC), pancreatic cancer, and several other types of cancer. The drug acts on the epidermal growth factor receptor as a receptor tyrosine kinase inhibitor. Resistance to Erlotinib is known to develop rapidly after treatment. In particular, resistance to Erlotinib in NSCLC has been studied by various authors, including Garvey et al. (2016); Mumenthaler et al. (2011, 2015). In this section, we consider the experimental data of Garvey et al. (2016); Mumenthaler et al. (2015) to set our model parameters and study the propagation of resistance to Erlotinib in NSCLC.

When subjected to low level of resources (Oxygen 1% and Glucose 0g/L) the growth rate of the sensitive NSCLC cells is 0.24/day. This rate increases to 0.84/day in a high resource environment (Oxygen 20% and Glucose 2g/L). Therefore, we take $a_1 = 0.84$ with $S_0 = 1$ indicating a high resource concentration. On the other hand, the growth rate of resistant cell is reduced by approximately 70%. Thus, we set $a_2 = 0.5385$. Experimentally, the cytotoxic effects of erlotinib are explored in the range 0.001 μM – 10 μM with both sensitive and resistant cells (see Figure 3 in Mumenthaler et al. (2015)). While the drug is effective to parental cells, it has almost no effect to resistant cells harboring the MET amplification form of resistance, particularly in high resource concentration. Therefore, we take the drug effect parameters as

$$b_1 = \begin{cases} 0.84c_1, & c_1 \le 1, \\ 0.04c_1 + 0.8, & c_1 > 1, \end{cases}$$

$b_2 = 6.833$, and $b_3 = 5 + c_1$, to approximate the data provided in Mumenthaler et al. (2015).

In the following results, we focus on comparing heterogeneous and homogeneous microenvironments. The heterogeneity of the microenvironment in Mumenthaler et al. (2015) is modeled using a weighted series of compartments reflecting drug, oxygen, and glucose levels disseminating from blood vessels within the tumor, which is similar to the diffusive infusion in our simulations. The homogeneous microenvironment is taken as the case of a constant infusion with the concentration being the average of the diffusive case.

Figure 30 compares the diffusive (heterogeneous) and constant (homogeneous) case in moderate and high drug dosages. We take the drug concentrations as $C_1 = 1.2$ and $C_1 = 4$, and the resource level as $S_0 = 1.2$ in the diffusive case, and their spatial average in the constant case. The initial condition assumes 1% of preexisting resistant cells, which is taken to be the sum of two Gaussian distributions (17) with mean 0.2 and 0.8, and normalizing constant C_Q with ratio 100 to 1. The initial density ρ_0 is taken as 0.01 with a uniform noise of magnitude 0.005 to resemble the tumor in Figure 5 of Garvey et al. (2016). As shown in Figure 30, when the drug concentration is low to moderate, the total number of cancer cells is substantially higher in the diffuse case compared with the constant resources case. The corresponding total number of cancer cells in the case of high drug concentrations shows significantly closer numbers. The mean resistance level $\mathrm{E}[n(t,x,\theta)]$ indicates that this is caused due to the resistant cells surviving in high drug concentration. However, in the diffusive case, we still observe larger variance compared with the constant case, which has a larger potential of tumor growth when the microenvironment changes.

In addition, we demonstrate that the optimal drug dosage considering the high-dose pulse schedule (Mumenthaler et al., 2015) differs depending on the heterogeneity of the microenvironment. The high-dose pulse can only be given for a period of time considering drug toxicity (Foo and Michor, 2009). Thus, the dose pulse from $C_1 = 1$ to $C_1 = 10$ is given for a time specified in the constraint provided in Figure 7 of Mumenthaler et al. (2015), and for the remainder of the treatment, a low dosage of $C_1 = 1$ is given. We consider a resource level $S_0 = 1.2$ in the diffusive case and $S_0 = 1$ in the constant case, and the initial condition assumes 0.1% of preexisting resistant cells. Figure 31 shows that the optimal drug dosage differs depending on the microenvironment, and the tumor growth is more sensitive to the high-dose pulse in the diffusive case, where the relapse size varies more severely depending on the drug

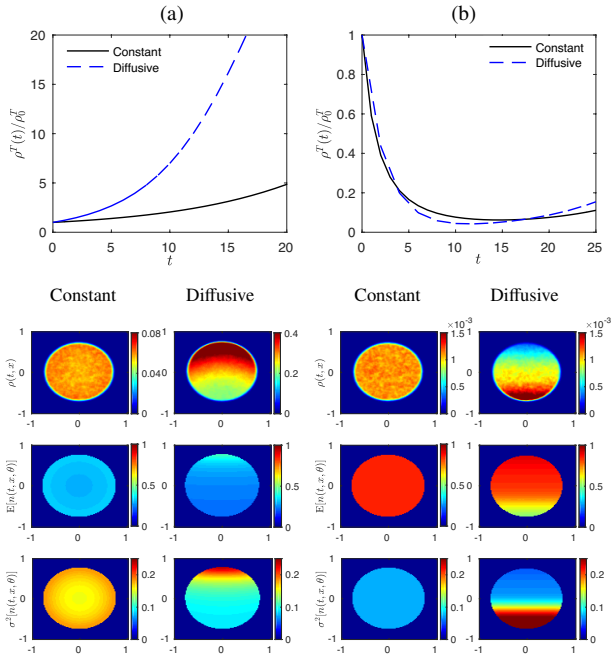

Figure 30: Comparison of tumor growth between constant and diffusive (homogeneous and heterogeneous in Mumenthaler et al. (2015)) in different drug concentrations, (a) moderate dosage, $C_1 = 1.2$ and (b) high dosage, $C_1 = 4$. The figures show total number of cancer cells $\rho_T(t)/\rho_T^0$, tumor density $\rho(t,x)$ at $t = 20$, and mean and variance of resistance level, $\mathrm{E}[n(t,x,\theta)]$ and $\sigma^2[n(t,x,\theta)]$ at $t = 20$. The trends of tumor growth in the constant and diffusive case become similar in high drug environment.

dosage. Hence, it is critical to include the heterogeneity in the microenvironment when designing optimal drug schemes.

8. Conclusion

In this paper, we developed a tumor growth model that describes the emergence of heterogeneous resistant cancer cells during chemotherapy. Tumor invasion is modeled by the pressure term that is inspired by the porous medium equation depending on the density of cancer cells. A diffusion term yields a smooth boundary resembling the proliferating rim. The growth term is restricted by the homeostatic pressure and the carrying capacity, which naturally gives rise to a necrotic region. In addition, the model incorporates the dynamics of the nutrients and two types of drugs: a cytotoxic drug that impacts the death rate, and a cytostatic drug that slows down the proliferation. This model extends the existing literature of heterogeneous resistance models (Cho and Levy, 2017; Lorz et al., 2015, 2013) to an asymmet-

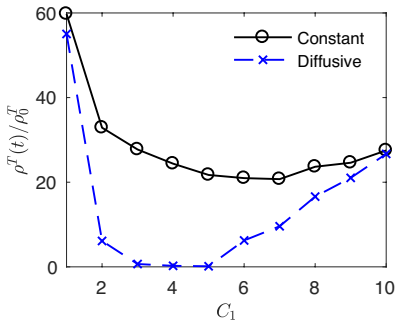

Figure 31: Total number of cancer cells $\rho_T(t)/\rho_T^0$ at $t = 28$ for different level of high-dose pulse C_1. The dosage that minimizes the tumor is less in the diffusive case than in the constant case, and the tumor size in the diffusive case is more sensitive to the dosage.

ric tumor growth model that significantly enhances the practicality of this approach and enables translational *in silico* exploration.

We test our model in various scenarios including spatially homogeneous case, diffusive infusion, and highly heterogeneous environment. The tumor behavior differs significantly depending on the environment and on the initial state of the tumor prior to the treatment. Our model demonstrates how multiple resistant traits can emerge at distinct locations. In particular, we consider NSCLC and its resistance to erlotinib using the data of Garvey et al. (2016); Mumenthaler et al. (2015). We demonstrate the importance of considering heterogeneous microenvironment and resistance levels.

In addition, we estimated the speed of propagation of the tumor boundary and the relapse time in terms of the dominant resistance trait and the concentrations of the nutrients and the drugs. Our model demonstrates that chemotherapy using the cytotoxic drug with strong intensity delays the cancer relapse, but yields highly resistant traits that cannot be eliminated with the cytotoxic drug only. Moreover, the on-off drug schedule results in more resistant traits compared with the constant drug infusion with the same total drug dosage in a given period. Finally, we propose a strategy of drug scheduling focusing on the elimination of the resistant cells. It consists of accurately combining the cytotoxic and cytostatic drugs. The effectiveness of such treatment is demonstrated in our simulations.

We would like to note that the model considered in this manuscript is a significantly extended version of the model we studied in Cho and Levy (2017). The main differences include: (i) Here we consider the spatially anisotropic two-dimensional case with a moving boundary, while the paper in Cho and Levy (2017) considered the radially symmetric case with a fixed boundary; (ii) Since we consider the full two-dimensional case, we can simulate the heterogeneous and asymmetric initial conditions and microenvironments from Mumenthaler et al. (2015); Peng et al. (2016). This was not possible with the previous radially symmetric toy model; (iii) The present work includes estimates of the expansion rate of the tumor boundary and of the relapse time; and (iv) An optimal drug strategy combining cytotoxic and cytostatic drugs is explored, showing that the most resistant trait can be eliminated using our proposed protocol.

Future work includes extending our model to vascularized systems (Anderson et al., 2006; Trédan et al., 2007) and combining it with complex microdynamics systems such as extracellular matrices and various proteolytic enzymes (Anderson, 2005; Chaplain et al., 2006; Deakin and Chaplain, 2013). This will lead to a multiscale model which requires an effective algorithm involving adaptive refinement at the tumor boundary, Peng et al. (2016). In addition, incorporating the healthy cells into the model will yield more interesting dynamics driven by the competition between the healthy and cancer cells (Lorz et al., 2015). In the regime of resistance modeling, we further aim to study the multi-drug resistance (Panagiotopoulou et al., 2010) by considering a multi-dimensional trait variable subject to different classes of drugs and other phenotypes. The most challenging work involves validating the parameters with available experimental and imaging data (Alexander et al., 2008; Weiger et al., 2013). Additional challenges include matching our continuum model with and also coordinating our continuum model with discrete and probabilistic models, e.g., agent based models, Byrne and Drasdo (2009), or game theoretic models, Kaznatcheev et al. (2017).

Appendix A. Estimation of tumor boundary speed

The tumor growth can be quantified using the estimation of the velocity of tumor boundary in the limit $k \to \infty$ (Kim et al., 2016; Mellet et al., 2015; Perthame et al., 2014). Let us consider a single resistant trait θ^* and assume a radially symmetric tumor, so that $\rho(t, r) = n(t, r, \theta^*)$. We follow the assumption in Perthame et al. (2014) that the initial condition satisfies $n(0, r) = n_0(r) > 0$ and $p(0, r) = \frac{k}{k-1} n_0(r)^{k-1} \le \bar{p}$, and the growth term (4) satisfies $G'(p) \le 0$ and $G(\bar{p}) = 0$. Then the limiting solution, when $k \to \infty$, denoted as n_∞ and p_∞, satisfies

$$\partial_t n_\infty - \nu_n \Delta n_\infty - \nu_p \Delta p_\infty = n_\infty G(p_\infty). \tag{A.1}$$

The asymptotic constant speed can be estimated as follows. Since the limiting solution is similar to an indicator function except at the boundary, we assume that the tumor at time t is a ball with radius $r(t)$ centered at the origin as $\Omega_0(t) = \{x \,|\, p_\infty(t,x) > 0\} = \{x \,|\, n_\infty(t,x) = 1\} = B_{r(t)}(0)$. We let $\rho_r(r - \mathsf{v}t) = n_\infty(t)$ and $p_r(r - \mathsf{v}t) = p_\infty(t)$, and substitute our ansatz in Eq. (A.1) to obtain

$$\mathsf{v} = -\nu_p p_r'(r(0)) + \nu_n(d-1)\int_{r(0)}^{\infty} \frac{n_r'}{r} dr + G(0)\int_{r(0)}^{\infty} n_r dr,$$

in d-dimensions. By using the complementary relation $p_\infty(\nu_p \Delta p_\infty + G(p_\infty)) = 0$, the first term becomes

$$-\nu_p p'(r(0)) \simeq \sqrt{2\nu_p \int_0^{\bar{p}} G(q)dq} = \sqrt{2\nu_p G^* \bar{p}},$$

where $G^* = r(\theta^*)S_0 - D(\theta^*)$.

Appendix B. Drug administration

We consider the time dependent drug administration with a period T_p, a treatment length T_d, and a half-life of drug T_h as $C_1(t) = C_1^b I_c(t)$. Here, C_1^b is the drug intensity, and $I_c(t)$ describes the temporal dynamics as

$$I_c(t) = \begin{cases} \frac{1}{A_1}(1 - 2^{-t}) + A_2, & t \in [0,\, T_d], \\ \frac{1}{A_3} e^{-\lambda_{c1} t}\left(e^{\lambda_{c1} T_d} - 1\right), & t \in [T_d,\, T_p], \end{cases}$$

where $\lambda_{c1} = \ln(2)/T_h$, $A_1 = (1 - 2^{-T_d})/(1 - A_3)$, $A_2 = e^{-\lambda_{c1} T_p}(e^{-\lambda_{c1} T_d} - 1)/A_1$, and $A_3 = 1 - e^{-\lambda_{c1} T_d}$. These constants are computed so that $I_c(t)$ is continuous and periodic on $[0,\, T_p]$. Figure 16(a) shows some examples of $C_1(t)$ with $C_1^b = 4$.

Acknowledgments

The work of DL was supported in part by the National Science Foundation under Grant Number DMS-1713109, by the Simons Foundation, and by the Jayne Koskinas Ted Giovanis Foundation. We would like to thank Antoine Mellet for useful discussions.

References

Alexander, S., Koehl, G. E., Hirschberg, M., Geissler, E. K., Friedl, P., 2008. Dynamic imaging of cancer growth and invasion: a modified skin-fold chamber model. Histochem Cell Biol. 130, 1147–1154.

Amir, E.-a. D., Davis, K. L., Tadmor, M. D., Simonds, E. F., Levlne, Jacob, H., Bendall, S. C., Shenfeld, D. K., Krishnaswamy, S., Nolan, G. P., Pe'er, D., 2013. viSNE enables visualization of high dimensional single-cell data and reveals phenotypic heterogeneity of leukemia. Nat Biotechnol. 31 (6), 545–552.

Anderson, A. R., 2005. A hybrid mathematical model of solid tumour invasion: The importance of cell adhesion. Math. Med. Biol. 22 (2), 163–186.

Anderson, A. R., Chaplain, M., 1998. Continuous and discrete mathematical models of tumor-induced angiogenesis. Bull. Math. Biol. 60 (5), 857–899.

Anderson, A. R., Weaver, A. M., Cummings, P. T., Quaranta, V., 2006. Tumor morphology and phenotypic evolution driven by selective pressure from the microenvironment. Cell 127 (5), 905–915.

Bellomo, N., De Angelis, E., Preziosi, L., 2003. Multiscale modeling and mathematical problems related to tumor evolution and medical therapy. J. Theor. Med. 5 (2), 111–136.

Bendall, S. C., Simonds, E. F., Qiu, P., Amir, E.-a. D., Krutzik, P. O., Bruggner, R. V., Melamed, R., Trejo, A., Ornatsky, O. I., Balderas, R. S., Plevritis, S. K., Sachs, K., Pe, D., Tanner, S. D., Nolan, G. P., 2011. Single-cell mass cytometry of differential immune and drug responses across a human hematopoietic continuum. Science 332 (6030), 687–696.

Birkhead, B. G., Rakin, E. M., Gallivan, S., Dones, L., Rubens, R. D., 1987. A mathematical model of the development of drug resistance to cancer chemotherapy. Eur. J. Cancer Clin. Oncol. 23, 1421–1427.

Bray, D., 2000. Cell Movements : From Molecules to Motility, 2nd Edition. Garland Science.

Brú, A., Albertos, S., Subiza, J. L., Asenjo, J. A., Brú, I., 2003. The universal dynamics of tumor growth. Biophys. J. 85, 2948–2961.

Byrne, H., Drasdo, D., 2009. Individual-based and continuum models of growing cell populations: A comparison. J. Math. Biol. 58 (4-5), 657–687.

Byrne, H. M., Alarcon, T., Owen, M. R., Webb, S. D., Maini, P. K., 2006. Modelling aspects of cancer dynamics: a review. Philos. Trans. A. Math. Phys. Eng. Sci. 364, 1563–1578.

Byrne, H. M., Chaplain, M. A., 1996. Growth of necrotic tumors in the presence and absence of inhibitors. Math. Biosci. 135, 187–216.

Byrne, H. M., Preziosi, L., 2003. Modelling solid tumour growth using the theory of mixtures. Math. Med. Biol. 20 (4), 341–366.

Calabresi, P., Schein, P. S., 1993. Medical Oncology : Basic principles and clinical management of cancer, 2nd Edition. New York : McGraw-Hill.

Casciari, J. J., Sotirchos, S. V., Sutherland, R. M., 1992. Variation in tumour cell growth rates and metabolism with oxygen-concentration, glucose-concentration and extracellular ph. J. Cell. Physiol. 151, 386–394.

Chaplain, M. A. J., Graziano, L., Preziosi, L., 2006. Mathematical modelling of the loss of tissue compression responsiveness and its role in solid tumour development. Math Med Biol 23, 197–229.

Cho, H., Levy, D., 2017. Modeling the dynamics of heterogeneity of solid tumors in response to chemotherapy. Bull. Math. Biol. accepted.

Corbett, T., Griswold, D., Roberts, B., Peckham, J., Schabel, F., 1975. Tumor induction relationships in development of transplantable cancers of the colon in mice for chemotherapy assays, with a note on carcinogen structure. Cancer Res. 35, 2434–2439.

Cristini, V., Frieboes, H. B., Li, X., Lowengrub, J. S., Macklin, P., Sanga, S., Wise, S. M., Zheng, X., 2008. Selected Topics in Cancer Modeling. Springer, Ch. Nonlinear modeling and simulation of tumor growth, pp. 113–181.

Cristini, V., Lowengrub, J., Nie, Q., 2003. Nonlinear simulation of tumor growth. J. Math. Biol. 46 (2), 191—224.

de Bruin, E. C., Taylor, T. B., Swanton, C., 2013. Intra-tumor heterogeneity: lessons from microbial evolution and clinical implications. Genome Med 5, 1–11.

de Pillis, L. G., Radunskaya, A. E., Wiseman, C. L., 2005. A validated mathematical model of cell-mediated immune response to tumor growth. Cancer Res. 65, 7950–7958.

de Pillis, L. G., Savage, H., Radunskaya, A. E., 2014. Mathematical model of colorectal cancer with monoclonal antibody treatments. Br. J. Med. Med. Res. 4, 3101–3131.

Deakin, N. E., Chaplain, M. A. J., 2013. Mathematical modelling of cancer cell invasion: the role of membranebound matrix metalloproteinases. Front. Oncol. 3 (2), 1–9.

Fodal, V., Pierobon, M., Liotta, L., Petricoin, E., 2011. Mechanisms of cell adaptation: when and how do cancer cells develop chemoresistance? Cancer J. 17 (2), 89–95.

Folkman, J., Hochberg, M., 1973. Self-regulation of growth in three dimensions. J. Exp. Med. 138, 745–753.

Foo, J., Michor, F., 2009. Evolution of resistance to targeted anticancer therapies during continuous and pulsed administration strategies. PLoS Comput Biol. 5, e1000557.

Foo, J., Michor, F., 2014. Evolution of acquired resistance to anticancer therapy. J. Theor. Biol. 355, 10–20.

Garvey, C. M., Spiller, E., Lindsay, D., Chiang, C.-t., Choi, N. C., Agus, D. B., Mallick, P., Foo, J., Mumenthaler, S. M., 2016. A high-content image-based method for quantitatively studying context-dependent cell population dynamics. Sci Rep. 6 (29752), 1–12.

Gatenby, R. A., Gawlinski, E. T., 1996. A reaction-diffusion model of cancer invasion. Cancer Res 56 (31), 5745–5753.

Gerlinger, M., Rowan, A. J., Horswell, S., Larkin, J., Endesfelder, D., Gronroos, E., Martinez, P., 2012. Intratumor heterogeneity and branched evolution revealed by multiregion sequencing. N. Engl. J. Med. 366, 883–892.

Gillet, J.-P., Gottesman, M. M., 2010. Mechanisms of multidrug resistance in cancer. Methods Mol Biol 596, 47–76.

Goldie, J. H., Coldman, A. J., 1979. A mathematical model for relating the drug sensitivity of tumors to their spontaneous mutation rate. Cancer Treat. Rep. 63, 1727–1733.

Goldie, J. H., Coldman, A. J., 1983a. A model for resistance of tumor cells to cancer chemotherapeutic agents. Math. Biosci. 65, 291–307.

Goldie, J. H., Coldman, A. J., 1983b. Quantative model for multiple levels of drug resistance in clinical tumors. Cancer Treat. Rep. 67, 923–931.

Gottesman, M. M., 2002. Mechanisms of cancer drug resistance. Annu Rev Med 53, 615–627.

Gottesman, M. M., Fojo, T., Bates, S. E., 2002. Multidrug resistance in cancer: Role of ATP-dependent transporters. Nat. Rev. Cancer 2 (1), 48–58.

Greene, J., Lavi, O., Gottesman, M. M., Levy, D., 2014. The impact of cell density and mutations in a model of multidrug resistance in solid tumors. Bull. Math. Biol. 74, 627–653.

Greenspan, H., 1976. On the growth and stability of cell cultures and solid tumors. J. Theor. Biol. 56 (56), 229—242.

Grothey, A., 2006. Defining the role of panitumumab in colorectal cancer. Community Oncol. 3, 6–10.

Grover, A., Sanjuan-pla, A., Thongjuea, S., Carrelha, J., Giustacchini, A., Gambardella, A., Macaulay, I., Mancini, E., Luis, T. C., Mead, A., Jacobsen, S. E. W., Nerlov, C., 2016. Single-cell RNA sequencing reveals molecular and functional platelet bias of aged haematopoietic stem cells. Nature Communications 7 (11075), 1–12.

Iwasa, Y., Nowak, M. A., Michor, F., 2006. Evolution of resistance during clonal expansion. Genetics 172, 2557–2566.

Kaznatcheev, A., Scott, J. G., Basanta, D., 2017. Edge effects in gametheoretic dynamics of spatially structured tumours. J. R. Soc. Interface 12, 1–7.

Kim, I. C., Perthame, B., Souganidis, P. E., 2016. Free boundary problems for tumor growth: A viscosity solutions approach. Nonlinear Anal Theory Methods Appl 138, 207–228.

Kimmel, M., Swierniak, A., Polanski, A., 1998. Infinite-dimensional model of evolution of drug resistance of cancer cells. J. Math. Syst. Estim. Control 8, 1–16.

Komarova, N., 2006. Stochastic modeling of drug resistance in cancer. Theor. Popul. Biol. 239 (3), 351–366.

Lavi, O., Gottesman, M. M., Levy, D., 2012. The dynamics of drug resistance: A mathematical perspective. Drug Resist. Updates 15 (1-2), 90–97.

Lorz, A., Lorenzi, T., Clairambault, J., Escargueil, A., Perthame, B., 2015. Modeling the effects of space structure and combination therapies on phenotypic heterogeneity and drug resistance in solid tumors. Bull Math Biol 77, 1–22.

Lorz, A., Lorenzi, T., Hochberg, M. E., Clairambault, J., Perthame, B., 2013. Populational adaptive evolution, chemotherapeutic resistance and multiple anti-cancer therapies. Esaim Math Model Numer Anal 47, 377–399.

Lowengrub, J. S., Frieboes, H. B., Jin, F., Chuang, Y.-L., Li, X., Macklin, P., Wise, S. M., Cristini, V., 2010. Nonlinear modelling of cancer: bridging the gap between cells and tumours. Nonlinearity 23 (1), R1–R9.

Macklin, P., Lowengrub, J., 2007. Nonlinear simulation of the effect of microenvironment on tumor growth. J. Theor. Biol. 245 (4), 677–704.

Macklin, P., McDougall, S., Anderson, A. R. A., Chaplain, M. A. J., Cristini, V., Lowengrub, J., 2009. Multiscale modelling and nonlinear simulation of vascular tumour growth. J. Math. Biol. 58, 765–798.

Mallett, D. G., De Pillis, L. G., 2006. A cellular automata model of tumor-immune system interactions. J. Theor. Biol. 239 (3), 334–350.

Mansury, Y., Kimura, M., Lobo, J., Deisboeck, T. S., 2002. Emerging patterns in tumor systems: simulating the dynamics of multicellular clusters with an agent-based spatial agglomeration model. J. Theor. Biol. 219 (3), 343–370.

Mcmaster, M. L., Kristinsson, S. Y., Turesson, I., Bjorkholm, M., Landgren, O., 2012. Tumor growth modeling from the perspective of multiphase porous media mechanics. Mol Cell Biomech. 9 (3), 193–212.

Melicow, M. M., 1982. The three-steps to cancer: a new concept of carcinogenesis. J. Theor. Biol. 94, 471–511.

Mellet, A., Perthame, B., Quiros, F., 2015. A Hele-Shaw problem for tumor growth, 1–25.

Michor, F., Nowak, M. A., Iwasa, Y., 2006. Evolution of Resistance to Cancer Therapy. Curr. Pharm. Des. 12, 261–271.

Minchinton, A. I., Tannock, I. F., 2006. Drug penetration in solid tumours. Nat. Rev. Cancer. 6, 583–592.

Mumenthaler, S., Foo, J., Leder, K., Choi, N. C., Agus, D. B., Pao, W., Mallick, P., Michor, F., 2011. Evolutionary modeling of combination treatment strategies to overcome resistance to tyrosine kinase inhibitors in non-small cell lung cancer. Mol. Pharm. 8, 2069—2079.

Mumenthaler, S. M., Foo, J., Choi, N. C., Heise, N., Leder, K., Agus, D. B., Pao, W., Michor, F., Mallick, P., 2015. The impact of microenvironmental heterogeneity on the evolution of drug resistance in cancer cells. Cancer Informatics 14, 19–31.

Panagiotopoulou, V., Richardson, G., Jensen, O. E., Rauch, C., 2010. On a biophysical and mathematical model of Pgp-mediated multidrug resistance: understanding the "space-time" dimension of MDR. Eur. Biophys. J. 39, 201–211.

Panetta, J. C., 1998. A mathematical model of drug resistance: heterogeneous tumors. Math Biosci. 147, 41–61.

Peng, L., Trucu, D., Lin, P., Thompson, A., Chaplain, M. A. J., 2016. A multiscale mathematical model of tumour invasive growth. Bull. Math. Biol. 79 (3), 389–429.

Perthame, B., Quirós, F., Vázquez, J. L., 2014. The Hele-Shaw asymptotics for mechanical models of tumor growth. Arch. Ra-

tional Mech. Anal. 212 (1), 93–127.
Preziosi, L., Tosin, A., 2009. Multiphase modelling of tumour growth and extracellular matrix interaction: mathematical tools and applications. J. Math. Biol. 58, 625–656.
Rainey, P. B., Travisano, M., 1998. Adaptive radiation in a heterogeneous environment. Nature 2, 69–72.
Roose, T., Chapman, S. J., Maini, P. K., 2007. Mathematical models of avascular tumor growth. Siam Review 49 (2), 179–208.
Simon, R., Norton, L., 2006. The norton–simon hypothesis: designing more effective and less toxic chemotherapeutic regimens. Nat. Clin. Pract. Oncol. 3, 406–407.
Swierniak, A., Kimmel, M., Smieja, J., 2009. Mathematical modeling as a tool for planning anticancer therapy. Eur. J. Pharmacol. 625 (1-3), 108–121.
Teicher, B. A., 2006. Cancer Drug Resistance. Humana Press, Totowa, N.J.
Tomasetti, C., Levy, D., 2010. An elementary approach to modeling drug resistance in cancer. Math. Biosci. Eng. 7, 905–918.
Trédan, O., Galmarini, C. M., Patel, K., Tannock, I. F., 2007. Drug resistance and the solid tumor microenvironment. J. Natl. Cancer Inst. 99, 1441–1454.
Vaupel P., Kallinowski F., O. P., 1989. Blood flow, oxygen and nutrient supply, and metabolic microenvironment of human tumors: a review. Cancer Res. 49, 6449–6465.
Vazquez, J. L., 2006. The Porous Medium Equation: Mathematical Theory. Clarendon Press.
Weiger, M., Vedham, V., Stuelten, C. H., K. Shou, M. H., Sato, M., Losert, W., Parent, C., 2013. Real-time motion analysis reveals cell directionality as an indicator of breast cancer progression. PLoS ONE 8, e58859.
Wu, A., Loutherback, K., Lambert, G., Estévez-Salmerón, L., Tlsty, T. D., Austin, R. H., Sturm, J. C., 2013. Cell motility and drug gradients in the emergence of resistance to chemotherapy. Proc. Natl. Acad. Sci. 110 (40), 16103–16108.
Zheng, X., Wise, S. M., Cristini, V., 2005. Nonlinear simulation of tumor necrosis, neo-vascularization and tissue invasion via an adaptive finite-element/level-set method. Bull. Math. Biol. 67 (2), 211–259.